Chapter 5

H I and diffuse X-ray in spiral galaxies

Having studied the effects of X-ray emitting hot intra-group medium (IGM) on the H I content of galaxies, the next step was to understand the relation of the cold gas (H I) content of the galaxy and the X-ray emitting hot inter-stellar medium (ISM). This chapter discusses a quantitative comparative study of the properties of the hot X-ray emitting ISM in spiral galaxies–its origin, its relation with the star formation rate of the galaxies, and the relation of this hot (X-ray emitting) gas and the cold (H I) gas in spiral galaxies. The work involves analysis of the archived Chandra data for a sample of 34 nearby spiral galaxies and also uses their single dish H I , IRAS FIR and 2MASS K-band data from the literature.

5.1 Introduction

The earliest method of classifying galaxies was based on how they looked in projection on the sky. Morphology, was the guideline to the famous Hubble sequence, where galaxies were divided in early type and late type categories. Spheroidal shaped galaxies, with large stellar systems, were named 'Ellipticals' and flatter systems, with stars in the spiral arms were called the 'Spirals'.

X-ray studies of nearby galaxies were first made possible by the Einstein Observatory back in 1978 [52]. This opened up a whole new area of study of the evolved component of the stellar population in a galaxy. The X-ray emission from a galaxy is the result of contributions from several kinds of sources, such as, X-ray binaries (low mass and high mass), supernova remnants, OB star clusters, other point sources and the hot component of the interstellar medium. The presence of a hot diffuse X-ray gas in galaxies has been predicted for decades. Yet, the limitation in the spatial resolution and the sensitivity of early X-ray telescopes, prevented a proper study of this hot (10^7K) gas, till the advent of the *Einstein Observatory*. Elliptical galaxies were thought to be purely stellar systems, till the Einstein Observatory saw significant amount of X-ray emission from them [44]. The presence of X-rays in ellipticals meant that they had an interstellar medium composed of hot gas. Later this hot component of the ISM was seen in spirals as well ([43], [117]).

Prior to the launch of the Chandra and XMM-Newton, this hot component could be studied only in a few nearby galaxies. It requires very good sensitivity to detect the low energy hot gas and high spatial resolution to remove the point source contribution to the hot gas. Thus, the launch of the X-ray telescopes like XMM-Newton and Chandra, which are sensitive enough to detect these hot haloes of gas around galaxies, opened up the opportunities to study this diffuse ISM component in details. Especially with Chandra's subarcsecond resolution, point sources can now be removed to much better accuracy and varied interesting morphologies of this diffuse gas are being revealed ([137], [45], [147]).

5.1.1 Origin of the diffuse X-rays in spirals

Studies on X-ray emitting spiral galaxies suggest that normal spirals emit X-rays in the soft X-ray ($\sim 0.1 - 3.0$ keV) band with luminosities of $\sim 10^{38} - 10^{42}$ erg s^{-1}. This emission originates from a combination of the integrated output of supernova remnants, accreting close binaries (low- and high-mass X-ray binaries), and hot gaseous diffuse emission [116]. The latter, i.e the diffuse hot gas is present either in the form of hot outflows or winds rising from the disks of the galaxies towards the halo [157], [137], or hot coronal phases of the interstellar medium (ISM), seen within more normal galaxies [15]. In the present work, we will concentrate only on the diffuse X-ray emission from spiral galaxies. Studies done so far indicate two possible origins of this hot gas in spiral galaxies.

Supernova powered

In galaxies that show signs of enhanced star formation, soft diffuse X-rays observed are believed to originate due to thermal emission from a kT $\sim$ 0.2 keV (T $\sim 10^7$ K) component of the ISM ([117], [138]) which is mostly powered by supernovae and winds from young massive stars. Massive stars have a profound influence over the baryonic component of the universe, through the return of ionizing radiation, and via supernovae (SNe), kinetic energy and metal enriched gas, back to the ISM, from which they form, usually called 'feedback'. The purely mechanical feedback from the SNe and stellar winds (commonly termed SN feedback) in the disk of star forming galaxies, can produce, via blow-out or venting of hot gas from the disk, tenuous exponential atmospheres of density scale height 4-8 kpc. Thus the soft thermal X-ray emission observed in the halos of the starburst galaxies is either this preexisting halo medium, which has been swept up and shock heated by the starburst driven wind, or wind material compressed near the walls of the outflow by reverse shocks within the wind ([137]). Since supernovae generates metals, the transport of this hot gas can give a clue towards the understanding of the metallicity evolution of galaxies. The morphology and quantity of hot X-ray emitting gas in these galaxies is therefore related to the problem of

understanding the scales (spatial and temporal) over which the metal enrichment takes place. X-ray emission associated with the spiral arms thus should carry information about local, relatively short timescale metallicity enrichment due to the movement of the spiral density wave, whereas, larger scale superwinds are more likely to be relevant to the enrichment of the intergalactic medium.

The connection of the X-ray emitting diffuse hot gas to the star formation activity of the galaxy has been observationally verified in several studies. Read & Ponman (2001) studied the diffuse gas in spirals using ROSAT observations of the galaxies and found a strong correlation of star formation and the presence of hot gas. This correlation was especially true for starburst galaxies [116]. Strickland et al. (2004) studied a sample of 10 galaxies, mostly starbursts, using Chandra observations, and confirmed the fact that at least for starburst galaxies, the diffuse hot gas found either in the disk or halo the spiral galaxies is closely related to its star formation rate [138]. Another work carried out by Tyler et al (2004) with the Chandra observations of 12 face-on spiral galaxies, revealed 0.1 $\sim$ 2 keV X-ray energy flux in the spiral arms of the galaxy to be correlated with that in the mid-infrared emission suggesting X-rays to be tracing the recent star formation in the galaxy [147].

Primordial origin of hot gas

There is one more explanation of the presence of this hot gas in spirals. Although most of the recent studies have revealed the presence of this hot gas in star forming galaxies ([137], [147]), there are cases where spirals with no significant star formation activity, have been detected to have this hot gas halo [115]. According to studies done on the estimates of the cosmic baryon fractions, defined as the ratio of baryonic mass to total mass in the Universe, it is understood that most of the baryons in the Universe are in a hot, diffuse state at the present epoch [7]. Cosmological simulations suggest that 30-40 per cent of all baryons in the Universe are in intergalactic filaments of shock heated gas at temperatures $10^6 K$ <T < $10^7 K$, known as warm/hot intergalactic medium, WHIM [26]. While most of this material are predicted to reside in structures of low overdensities, outside the dark matter halos of

individual galaxies, a decent amount of this gas could also be in a form of extended halos of hot gas ($\sim 10^6K - 10^7K$) around individual galaxies, including spirals [47]. In fact the mass of this gas can be as much as the total mass of stars and cold gas in a galaxy [133]. Studies also indicate that galaxies accrete gas directly from these filaments [120]. The idea that disk galaxies are embedded in such halos of hot gas, dates back to the to the late fifties [134]. In this model, galaxy dark matter halos are continuously growing by the spherical accretion of gas along with dark matter. During the infall into the dark matter potential, the gas is heated, potentially to the halo virial temperature, later cooling radiatively. If the cooling is rapid, as is the case for T $< 10^6K$ gas, indicating shallow potential well, no accretion shock develops outside the evolving galactic disk. Thus according to this model, spirals with total mass $< 10^{11}M_\odot$, will accrete cold gas, non X-ray emitting gas [13]. At higher galaxy masses, thereby deeper potential wells, the accreted gas will emit in X-rays, giving rise to a halo like feature. Over the years, this general picture has been supported by observational and simulation studies. Cosmological simulations by Toft et al (2002) [143], showed the X-ray luminosity of the hot halo to scale strongly with disk circular velocity, indicating higher possibility of the presence of this hot halo in massive galaxies.

Observational evidence of halo gas in non star-forming galaxy has been seen recently [115]. For the first time, NGC5746, a massive spiral, with circular velocity ~ 318 km/s, with a fairly quiescent SFR ~ 0.8 $M_\odot$ per year, has been detected with an extended (upto 20 kpc above the disk) X-ray halo [115].

5.1.2 Motivation of the present study

This project is a comparative study of the hot ISM in a sample of spiral galaxies. The sample includes normal galaxies, starbursts and AGN host galaxies. Archived data for a sample of 34 galaxies, observed with Chandra have been analysed in an uniform manner to do this comparative study. The aim of this study is to address issues regarding the origin of the hot diffuse X-ray gas, its relation with star formation in the disk and/or the baryonic mass

of the galaxy, the effect of cold gas on the hot gas and whether the X-ray properties of the normal galaxies are different from the galaxies hosting AGN or starburst galaxies. A brief introduction to the issues to be addressed in this work is given below.

Origin of the diffuse gas: relation with star formation An important issue to address in this large sample of galaxies, is to identify the origin of the diffuse X-ray emission in these galaxies. As has been described above, the hot diffuse X-ray halo in a spiral can originate either from the heated accreted halo gas or can be supernovae powered, an effect of intense star formation in the disk. There exists only two previous statistical studies probing the origin of hot gas in spirals. The first study of this nature was carried out by Read & Ponman in 2001, with a sample of 17 galaxies, with ROSAT-PSPC data [116]. Their main conclusions regarding the nature of this emission and its relation with star formation in the disk were the following [116],

- In general, the X-ray properties of normal galaxies are governed by the galaxy size, whereas the X-ray properties of starburst galaxies are governed by the galaxy activity (in this case star formation).

- Larger normal galaxies contain more hot gas per unit mass than smaller ones. This is interpreted to be resulting from better retention of hot gas in the deeper potential wells of larger galaxies.

- In contrast, the diffuse emission per unit mass from starburst galaxies scales with activity rather than galaxy size. This is consistent with the idea that the hot gas in these systems is substantially unbound, and its density is therefore determined by the rate of hot gas production rather than by the retaining potential.

However this dataset suffered from the poor resolution of ROSAT, as proper removal of point sources is an important issue in estimating the diffuse emission. After the arrival of the Chandra Observatory, the next and a very elaborate study of the statistical properties of the diffuse gas in spirals was conducted by Strickland et al (2004)[138], with a sample of

10 galaxies, mostly starbursts. Their conclusions were similar to those of Read & Ponman (2001). They studied all edge on systems, concentrating their discussion mostly on the origin of the extraplanar halo diffuse X-rays. Among the results that came out of their study, the ones relevant to the present work are [138],

- The extraplanar (i.e., halo region) diffuse X-ray emission in the starburst galaxies is ultimately driven by SF activity within the disk, i.e., through starburst-driven superwinds.

- In both the starburst and normal spiral galaxies, larger galaxies show more radially and vertically extended diffuse X-ray emission, but beyond this correlation there is no evidence that galactic mass plays any part in determining the diffuse hot phase in the disks and halos of these galaxies.

- The extent of the diffuse X-ray emission parallel to the plane of the host galaxy correlates well with estimates of the extent of SF within the disk, further evidence that the soft thermal X-ray emission is a result of mechanical energy feedback from massive stars.

This study was very detailed and robust, but the sample size was only 10, with 7 starbursts and 3 normal galaxies. Thus a followup with a larger sample was necessary to validate their results, and search for the various factors responsible for such correlations.
Therefore at this point it was necessary to revisit the problem, with a bigger sample (consisting of normal galaxies, galaxies hosting AGNs and starbursts) and making use of the subarcsecond resolution of the Chandra, to get better understanding of the relation of the hot gas with star formation in the disks of the galaxies.

Hot gas and cold gas in spiral galaxies: Our next interest was to understand the relation of the H I content and deficiency of the galaxies to its hot gas content. In the first part of this thesis, we studied the effects of the group environment, in particular the hot diffuse medium (IGM) of the X-ray bright non-compact groups, on the H I content of galaxies. Spiral galaxies

in cluster cores are well known to be atomic hydrogen (H I) deficient. They move through the dense hot cluster cores with high velocities and lose gas through ram pressure stripping [58]. The hot (10^8 K) medium (ICM) can also strip gas from the galaxy through evaporation [34]. While cluster galaxies have been extensively studied, not many studies existed about the gas content and gas deficiency of the galaxies in groups and the possible gas removal processes that can work in such environments. In the first chapter of this thesis, we have discussed a comparative single dish study of the H I contents of non-compact groups with and without the hot IGM, indicating that the X-ray emitting medium may play a significant role in removing gas from the galaxies, as galaxies in these groups are found to be more H I deficient than the galaxies in groups without X-rays [125]. In the second chapter of this thesis, details of the H I imaging of some spirals of X-ray bright groups have been discussed. To see if the hot IGM is responsible for gas stripping from these galaxies, 13 galaxies from 4 X-ray bright groups were imaged in H I with the Giant Metrewave Radio Telescope (GMRT). Disturbed H I morphology was seen in some cases but most galaxies were seen to have a shrunken H I disk. This indicated that ram pressure may have stripped gas from the outer edges of the galaxies [126].

Having studied the effects of the environment (IGM) on the H I content of galaxies, the next step was to know the relation of the cold gas content of the galaxy and the X-ray emitting hot inter-stellar medium (ISM). Thus with this sample of galaxies, we studied the correlation of the diffuse X-ray luminosity with the H I mass and the H I deficiency of the galaxies.

The most widely applied relation between the observable properties of a galaxy and its star formation rate, remains the simple gas-density power law introduced by Schmidt (1959) [122], which for external galaxies is usually expressed in terms of the observable surface densities of gas and star formation.

$$\sigma_{SFR} = A{\sigma_{gas}}^{N} \tag{5.1}$$

Several observational studies have confirmed this. Mirabel and Sanders (1988) [92], sug-

gested a loose correlation of far-infrared luminosity with the H I mass of the galaxy. Kennicutt (1998), found a relation between the disk-averaged SFR surface density (σ_{SFR}) and average total (atomic plus molecular) gas density (σ_{gas}) using Hα, H I and CO observation for a sample of 61 galaxies [79]. A clear correlation was seen in the expected sense of increasing SFR with increasing gas densities in normal galaxies, though the scatter was large. He found the SFR versus H I density relation for 88 galaxies, to be very similar to the SFR versus total density relation, which is not surprising as H I accounts for almost half the total gas content of a galaxy. However, the physical interpretation of the SFR versus H I Schmidt law is not so obvious. It can either be the gas density influencing the SFR or it is also possible that SFR regulates the density of H I through the photodissociation of molecular gas by hot stars [127]. There have been some more recent studies conforming the correlation of H I and SFR [41], [86]. The H I mass and SFR has been seen to be related by the following equation,

$$log(HImass) = 0.59log(SFR) + 9.55 \tag{5.2}$$

This relation was estimated for the local universe, and Lah et al 2007 [86] showed that it holds for z=0.2 galaxies as well, suggesting that there has been no change in the star formation mechanisms ~3Gyrs ago: that the same amount of atomic hydrogen gives the same measurable SFR.

Thus it was interesting to examine how H I content of a galaxy varies with its diffuse hot gas content as this gas is primarily considered to be supernova powered and therefore can be connected to the star formation rate of the galaxy. Apart from seeing the behavior of this gas in the entire sample of galaxies, the idea was to divide the sample in categories like normal and AGN hosts and starbursts and study the similarities and/or differences in the behavior of the hot gas with respect to parameters like H I mass, H I deficiency, SFR, IR luminosity, K-band luminosity etc.

5.2 Data Analysis

5.2.1 Source Selection

The nature of this work, as mentioned above, requires a sample of spirals with varied range of properties like star formation rate, mass, HI mass etc. The sources were selected in the following way. A list was made of all the nearby galaxies from the Catalog of Nearby Galaxies by Tully & Fisher (1988) [146], either isolated or in group ($N_{grp} < 25$ to avoid clusters), between distances 10 to 35 Mpc, of morphological type 'T' 1 to 8 [40], and absolute blue magnitude $M_B \leq$ -18.5, and galactic latitude $|b| \geq 10$ deg. A subset of this list has been observed by the Chandra Observatory for various purposes.

Observations of as many galaxies as possible from this list were collected from the Chandra archives (as in August 2006). Only ACIS-I or S observations of duration > 15 ks, suitable for diffuse emission study were chosen from the subset to be analysed once more for this work. The aim of analysing the Chandra data was to make a uniform sample of analysed X-ray data of the spiral galaxies. Many of these galaxies have been analysed and published earlier, but since different authors use different energy ranges and different physical extents to get the diffuse X-ray luminosity of a galaxy, the entire sample needed a reanalysis for this work.

Table 1 lists the galaxy names, J2000 coordinates, optical radial velocity, distance to the galaxy, optical diameter, morphological type and an accompanying comment about the presence of absence of an AGN (N–normal, A–AGN). Table 2 lists important information about the Chandra observations of the sources: name, observation ID, date of observation, actual exposure time, detector type and data mode of the observation.

5.2.2 The Chandra Observatory

The Chandra X-Ray Observatory (CXO) (figure 1), combines an efficient high-resolution (~ 0.5 arcsecond) X-ray telescope with advanced imaging and spectroscopic instruments. Chan-

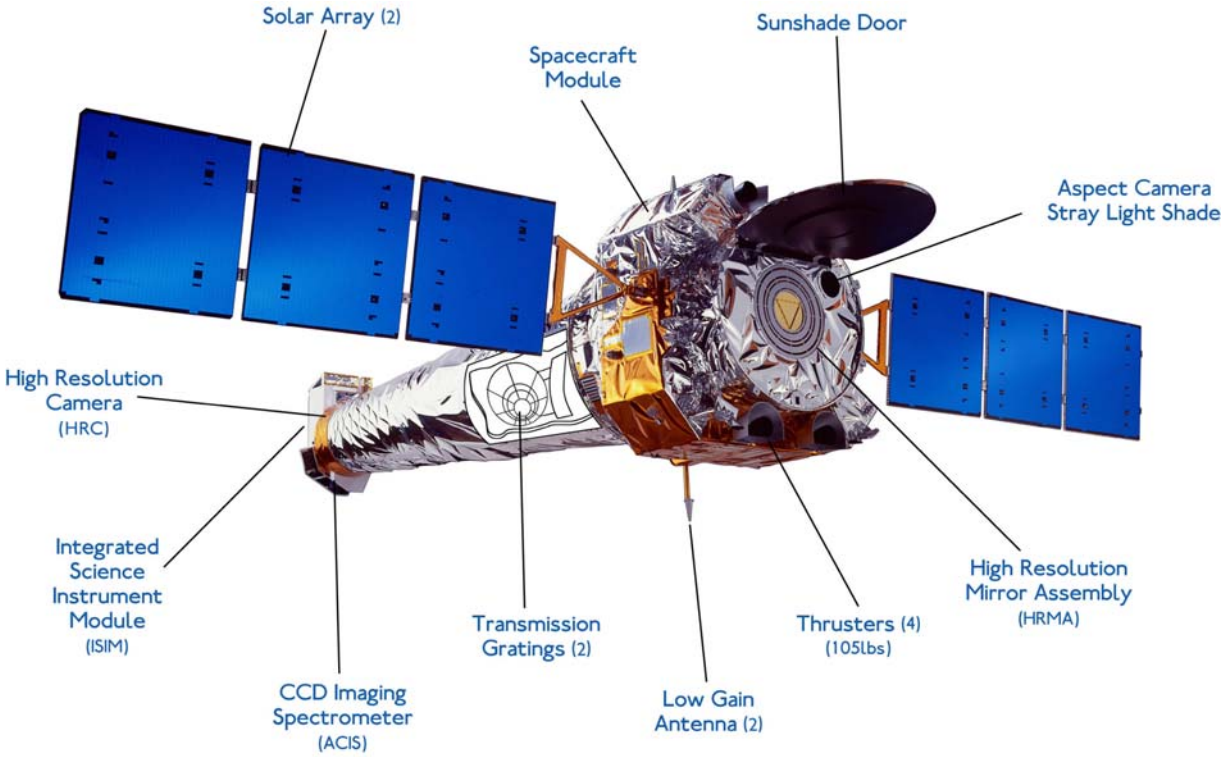

Figure 5.1: Chandra Observatory

dra was designed to provide order-of-magnitude advances over previous X-ray astronomy missions in terms of spatial and spectral resolution. The High Resolution Mirror Assembly (HRMA) produces images with a half-power diameter (HPD) of the point spread function (PSF) of < 0.5 arcsec.The HRMA consists of a nested set of four paraboloid-hyperboloid (Wolter-1) grazing-incidence X-ray mirror pairs, with the largest having a diameter of 1.2 m (twice that of the Einstein Observatory). The focal length is 10 m.

The Pointing Control and Aspect Determination (PCAD) system controls the pointing and dithering of the observatory and provides the data from which both the relative and absolute aspect are determined. Dithering is imposed in order to spread the instantaneous image over many different pixels of the focal plane detector to smooth out pixel-to-pixel variations. The dither pattern is a Lissajous figure. The amplitude, phase, and velocity depend on which instrument (ACIS or HRC) is in the focal plane.

The Chandra orbit is highly elliptical and varies with time. As of December 2006 the apogee

height was ~ 122,500 km and the perigee height was ~ 26,300 km. The apogee and perigee have been drawing closer to each other since launch and have now passed the turning point (minimum eccentricity). Over the next ~ 5 years the the apogee and perigee heights will draw apart again (at an average rate of a few thousand km/year). The orbit allows for reasonably high observing efficiency as the satellite spends most of the time well above the radiation belts (~ 75%) and long continuous observations (~ 160 ksec) are made possible by the orbital period of 63.5h.

The data used in this work were observed with the Advanced CCD Imaging Spectrometer (ACIS) of the Chandra. ACIS contains 10 planar, 1024 x 1024 pixel CCDs ; four arranged in a 2x2 array (ACIS-I) used for imaging, and six arranged in a 1x6 array (ACIS-S) used either for imaging or as a grating readout (figure 2). Two CCDs are back-illuminated (BI) and eight are front-illuminated (FI). The response of the BI devices extends to energies below that accessible to the FI chips. The chip-average energy resolution of the BI devices is better than that of the FI devices. Currently any combination of up to 6 CCDs can be operated simultaneously. Majority of the data used here are from the ACIS-S configuration of the detector. The ACIS-S array can be used with or without a grating. The back illuminated CCDs are more sensitive to soft X-rays than the I array CCDs. The data were acquired in Timed Exposure Mode, which is the mode with the default nominal (and optimal) frame time of 3.2s, is the typical mode for ACIS observations. The point-source sensitivity of the ACIS detector is $4 \times 10^{-15} ergcm^{-2}s^{-1}$ in10^4seconds.

5.2.3 Data Reduction

5.2.3.1 Data Preparation

The aim of this analysis was to create an uniform sample of spirals, all analysed in the same way. Therefore, all the galaxies discussed here were made to undergo the same analysis

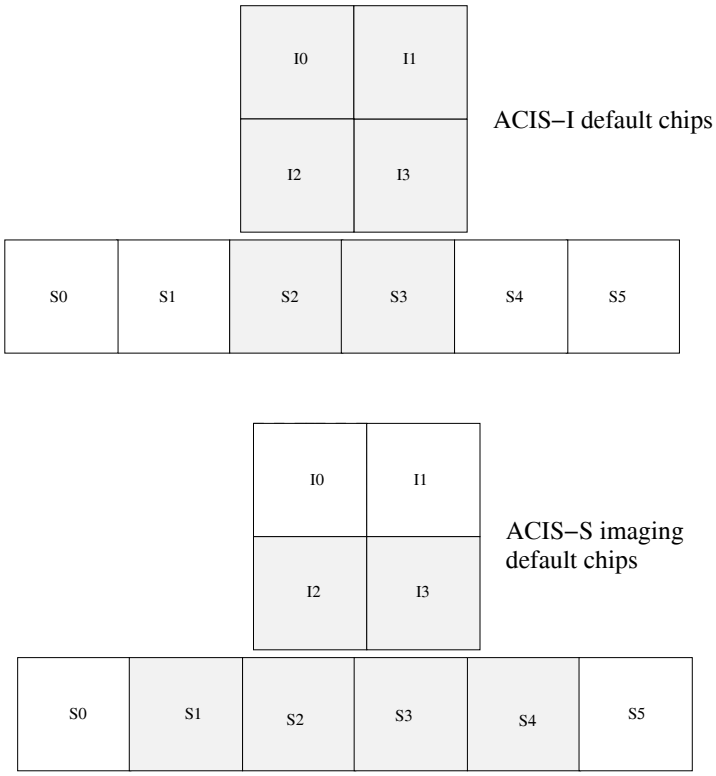

Figure 5.2: Arrangement of the ACIS chips; shaded part is the default configuration.

procedure described below.

The processes from the software CIAO, were used to reduce the data. First the data were subjected to the Standard Data Processing (SDP) of the Chandra. This was essentially cleaning of the data of bad pixels and bad times, and calibrating the data for future use. When Chandra data goes through SDP, or the pipeline, the most recently available calibration is applied to it.

The data were cleaned of bad pixels using the bad pixel map provided by the reduction pipeline, and calibrated using the 'ACIS-PROCESS-EVENTS' tool. Running ACIS-PROCESS-EVENTS with the level=1 event file as the input, produces a new level=1 event file that has the latest calibration applied. This means that the newest gain map will be picked up. In addition, one applies the pixel and PHA randomization and the ACIS charge transfer inefficiency (CTI) correction; all of these are part of standard data processing (SDP) and are "on" by default in ACIS-PROCESS-EVENTS (for more details please refer :http://asc.harvard.edu/ciao/guides/acis-data.html). The time-dependent gain correction

is also turned on by default, so it will be included in the processing. The time-dependent gain and CTI corrections are only applicable to -120 C data, but it is also left on for other temperatures; acis-process-events simply issues a warning in that case.

Next step for this new level=1 event file, was to filter it based on grade and status to create a level=2 event file. In general, the data were filtered to remove events that did not have a good GRADE (we excluded ASCA grades 1,5,7 here) or that had one or more of the STATUS bits set to 1 (for more details please refer:http://asc.harvard.edu/proposer/POG/html/ACIS.html-sec:GRADES).

Then the data were filtered to remove periods of anomalous background levels, such as the flares seen in ACIS observations.The ACIS background consists of a relatively soft Cosmic X-ray Background contribution and cosmic ray-induced events with a hard spectrum. These components change very slowly with time and can be predicted well (although they cannot be separated at present). There is an occasional strong third component producing background flares. These periods of high background were filtered using a 3σ clipping of the 0.2 to 10 keV lightcurves extracted in off-source regions, in 200 second bins.

While ACIS reads out a frame, it is still taking data. Photons detected during the readout are clocked out in the wrong row and so have incorrect CHIPY values. For a bright source, one gets a streak along the entire column of the source. Events above a source occur when a frame is being read out. Events below the source occur when the previous frame is being read out. In some cases this problem of ACIS Readout Streak was present and this streak was removed using the tool 'ACISREADCORR'.

The file cleaned in the above mentioned manner, creating a final events=2 file in the process, was used for all future imaging and spectral studies. Diffuse emission images were made from these events files, filtered to an energy range 0.3 to 2 keV.

5.2.3.2 Creating a diffuse emission image

For one normal galaxy, without any strong AGN, the entire process of creating a diffuse emission image is described below. The following four steps are to be followed in order to get a map of the diffuse emission. Details are described below. For all the galaxies used in this work the same processes were used to get the final images. The example of NGC278, a normal spiral, has been used to demonstrate the data analysis steps.

- To Identify and Remove Point Sources
- Filling in the Holes
- Exposure-Correcting the Image
- Smoothing the Image

The event file was filtered to an energy range 0.3 to 2 keV, and was converted to an image file by binning in pixels. The task 'WAVDETECT', a wavelet-based source detection tool, was run to identify the point sources. This task identified and marked the point sources as ellipses containing > 99.7 % (till 4σ) of the source counts. In some occasions, wavdetect was not efficient enough to identify all the point sources and/or sometimes it wrongly identified clumps of diffuse gas as point sources. For this purpose after every run of wavdetect, the point source region file was manually checked and corrected. The left panel of figure 3 shows the detected point sources for the observation of NGC278.

The point sources found thus were eliminated and the holes were filled with the emission from the corresponding background regions, using the task 'DMFILTH'. The background emission was derived from annulus shaped regions about the point sources. The right panel of figure 3 shows the background regions in the observation of NGC278. The background region files needed manual editing of the regions in order to avoid overlapping of a background

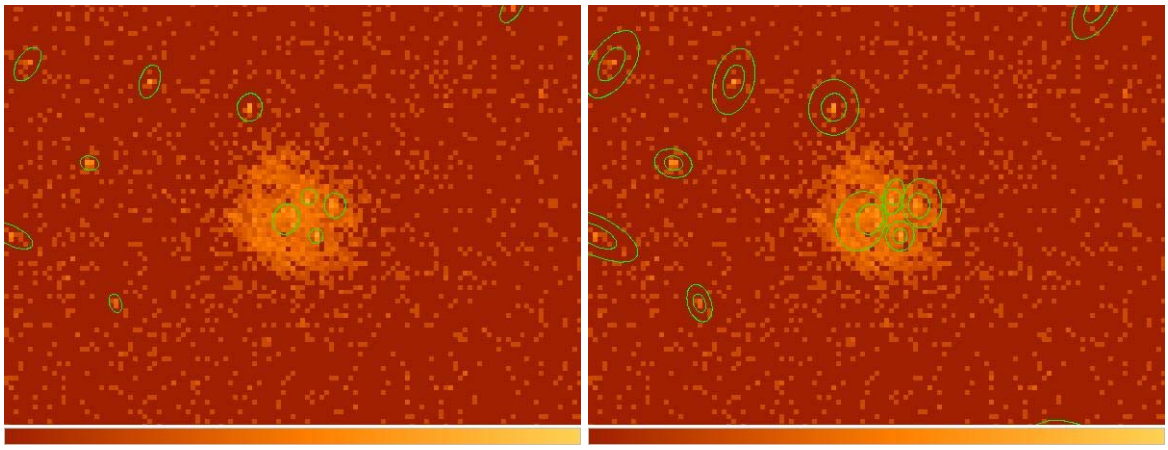

Figure 5.3: Left panel: The ellipses in green, denote the point sources; Right panel: The annuli in green are the background regions

region with a nearby source region and more than one iteration of the programs 'WAVDETECT' and subsequently 'DMFILTH' was necessary to detect all the point sources.

An important thing to note here is that in the cases where the galaxy harbours an AGN, the diffuse emission image was produced with the presence of the central AGN in some special cases. An effort to subtract it in the above manner and filling the holes with the background emission created unrealistic maps. Therefore the AGN was retained for the mapping purpose, which is to be noted, serves mostly illustration purposes and are not used for any quantitative analysis. However, while determining the flux of the diffuse emission, all the point sources including the AGNs were removed from the event files.

The filled image was then exposure corrected. An exposure map can be used to convert a counts image of a source to an image in flux units. The computed exposure map is essentially an image of the effective area at each sky position, accounting for the effects of dither motion which are especially important near the edges of the detector. A script 'MERGE-ALL' was used to create the exposure map. Finally the filled in and exposure corrected map was smoothed using the program 'ACONVOLVE'. This task convolves an N-dimensional image with a kernel (specified by the parameter 'kernelspec'). The kernel can be specified in one of several flexible ways: as either a file (image), a function, from the library, or specified on the

command line. One of the most common applications of this tool is smoothing of an image by convolving with a gaussian, which has been done for all of the sample galaxies. Figure 4, left and right panels represent the dmfilled, exposure corrected un-smoothed image and the final smoothed image respectively.

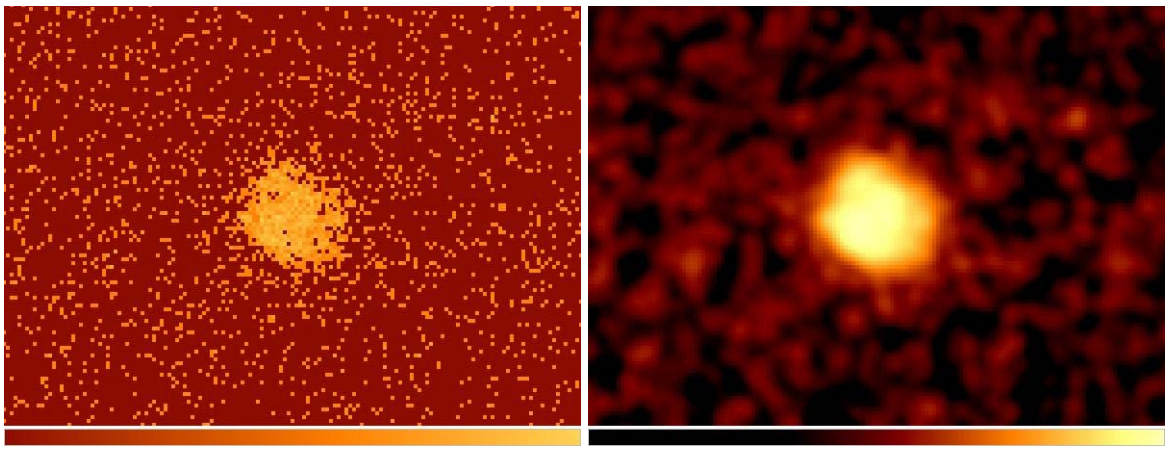

Figure 5.4: Left panel: exposure corrected unsmoothed image; Right panel: the exposure corrected image in the left panel is smoothed.

5.2.3.3 Hot plasma model

The diffuse hot gas in spiral galaxies is an optically thin $\sim$ 0.2 keV plasma that radiates a combination of thermal bremsstrahlung and line emissions. Because of relatively low temperatures, the entire gas is not completely ionised and therefore line emissions become an important factor here, along with thermal bremsstrahlung emission. The emission spectra from this hot diffuse gas was fitted (using the software XSPEC) with the model calculations of Mewe and Gronenschild (MEKA : as amended by Kaastra) [90]. A power law was added to the Meka model to take into account the unresolved pont source contribution. The flux obtained through this model fitting was contaminated with the contribution from unresolved point sources. However, the next subsection describes in detail, how this point source contamination was later removed from the estimated X-ray luminosities.

5.2.3.4 Unresolved Point Source Contribution

Study of diffuse X-ray emission from galaxies has always been a tricky subject because of the presence of numerous point sources in the galaxy. Even if the Chandra has the highest spatial resolution amongst all the X-ray telescopes launched so far and excellent sensitivity limits, this problem still persists to some extent. There are the faint unresolved sources, beyond the detection limit of the telescope which contaminates the diffuse flux. Contribution from these sources needs to be removed in order to get actual diffuse flux.

In these star forming galaxies, while the 0.3 to 2 keV gas is heated by the dying stars, the net X-ray in the 2 to 10 keV energy range is mostly contributed by the X-ray binaries. Recent studies of the X-ray emission from these galaxies have established a tight correlation of the X-ray luminosity to the star formation rate of the galaxy. Chandra observations of nearby star-forming galaxies and studies of high-mass X-ray binary (HMXB) population in the Milky Way and the Small Magellanic Cloud (SMC), led Grimm et al.(2003) [57] to propose that HMXBs can be used as a star formation rate (SFR) indicator. They found that, in a broad range of star formation regimes and rates, the X-ray luminosity (L_X) distribution of HMXBs can be approximately described by a 'universal' luminosity function: a power law with a slope of 1.6 and a cut-off at log(L_X)$\sim$ 40.5, the normalization of which is proportional to the SFR. As the 2−10 keV luminosity L_X of a normal galaxy with sufficiently high SFR/M* ratio (where M* is the total stellar mass) is dominated by the emission from HMXBs, the X-ray luminosity can be used as a SFR indicator for these galaxies.

The cumulative form of the 'universal' luminosity function of HMXBs in spiral galaxies, as derived by the authors was

$$N(>L) = 5.4 \times SFR \times ({L_{38}}^{-0.61} - 210^{-0.61}) \tag{5.3}$$

where L_{38} is luminosity value divided by 10^{38} and SFR denotes the star formation rate of the galaxy.

Though the contribution from these stars dominates the 2-10 keV band of X-rays, they can contaminate the 0.3-2.0 keV energy range as well, as the emission in this range by the hot

gas is already very faint. The contribution from the low luminosity sources which otherwise go undetected by the point source detecting softwares, can be calculated using the above luminosity function provided the SFR of the galaxy is known.

5.2.3.5 Diffuse Luminosity and the removal of unresolved point source contribution

The diffuse flux of a galaxy was derived from its 0.3 to 2 keV event=2 files. From the diffuse image, the physical extent to which the emission falls off to a 3 σ level were noted for the galaxy. The images used for this purpose were all low resolution images, smoothed to 20". The green contour about the galaxy in the right panel of figure 5 shows this region for NGC278. This contour was fitted with a circle, to estimate the diameter, to quantify the extent of the diffuse gas. For NGC278 this is 1.46′ . The white circle in the same figure defines the D_{25} diameter. Spectra from this 1.46′ region, eliminating the point sources within the region, was modeled in XSPEC with MEKA + power law, (power law to take into account the unresolved point sources and spillover radiation from the AGN if any) and the flux and thereafter the diffuse X-ray luminosity was derived. The values of total galactic H I column density, redshift of the galaxies were provided as the frozen parameters while fitting the models. The abundance parameter was set to 1 for all galaxies. The same procedure has been followed for all the galaxies and the diffuse X-ray luminosity of all these galaxies have been found in the above mentioned way.

To remove the contamination from the unresolved sources the following procedure was applied to all the galaxies in the sample. The clean event=2 file described in section 1.2.3.1, was filtered in energy range 0.3 to 8 keV. The ciao task 'WAVDETECT' was used to find and list all the point sources present in the chip with contains the galaxy. The source with minimum count was modeled in XSPEC with an absorbed power law with a fixed index of 1.8 [141]. This was assumed to be the luminosity lower limit for that particular observation. Since the galaxies in the sample are all spirals it was assumed that the main contribution to this unresolved point source flux will come from the high mass X-ray binaries. The cumula-

tive form of the universal HMXB luminosity function, as found by Grimm et al [57] (see eqn. 3) was used to get the contribution from sources which were below the minimum luminosity point source detected in the chip.

The SFR (star formation rate) values were calculated using FIR luminosities using 60 and 100 micron IRAS fluxes ($S_{60_{\mu m}}$ and $S_{100_{\mu m}}$ respectively in eqn. 4) ([131], [118], [121], "The Faint Source Catalog, version 2.0, Moshir et al. 1990). The formulae (from [116], [56] respectively) used were,

$$L_{FIR} = 3.65 \times 10^5 [2.58 S_{60_{\mu m}} + S_{100_{\mu m}}] \times D^2 L_{\odot} \tag{5.4}$$

$$SFR(M \odot yr^{-1}) = 4.5 \times 10^{-44} L_{FIR} \tag{5.5}$$

where D is the distance to the galaxy.

The contribution of X-ray point sources with luminosity values below the chip minimum luminosity value in the 0.3 to 2 keV range, was estimated and subtracted from the diffuse luminosities estimated in this energy range. For the galaxies where IRAS data were unavailable to calculate SFR and hence the unresolved point source contribution (NGC3507, NGC4485 and NGC7727), final diffuse X-ray luminosity values have been quoted assuming 10% of the diffuse luminosity to be contributed by the unresolved point sources. This approximation is based on an overall estimate of the ratio of the unresolved point source contribution to the diffuse luminosity in the 0.3 to 2 keV band.

Tables 3 lists the galaxy names, the angular radius to the 3 σ contour of the diffuse emission, the centre of the fitted circle to the 3 σ contour of the emission, the contribution from the unresolved sources and the final diffuse X-ray luminosity value of the galaxy with errorbars.

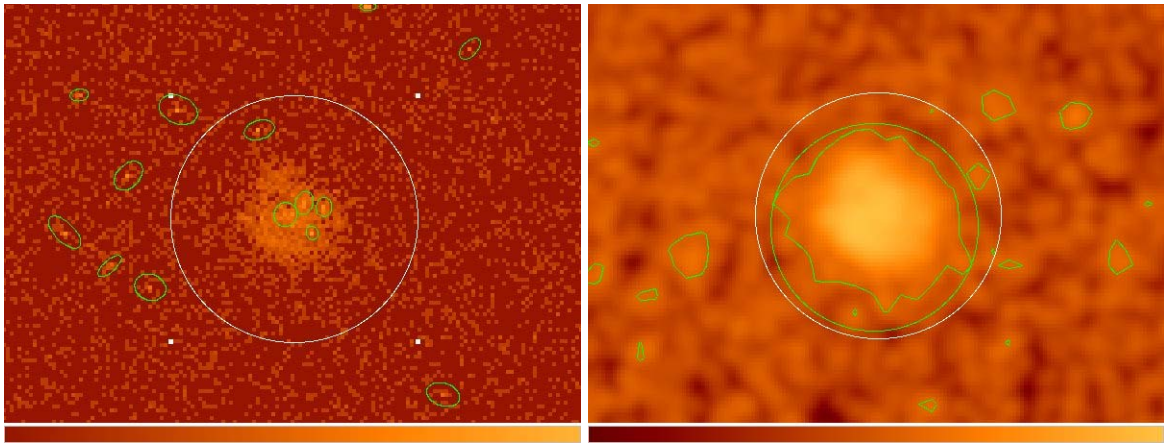

Figure 5.5: Left panel: The green ellipses denote the point sources and the diameter to the white circle is the D_{25} diameter; Right panel: Dmfilled, exposure corrected, smothed image of N278; the green contour surrounding the galaxy is the 3 σ contour of the diffuse emission, the green circle is a fit to the contour, and the white circle is the circle with D_{25} as its diameter.

5.3 Results

Since X-ray morphology is not our prime interest for carrying out this analysis, low resolution (~ 20") images of all 34 galaxies, obtained from the analysis of Chandra data, along with the hot plasma model fits to the spectrum of their diffuse emission are displayed in section 5.6 towards the end of this chapter. An accompanying table lists the fit parameters to the diffuse spectrum for each galaxy. However, a selected subsample of high resolution (~4") images of 6 galaxies are presented in this section. We will now move on to a quantitative comparative multiwavelength study of the diffuse X-ray properties of the sample galaxies. In this section, we attempt a statistical study on them to understand the following questions:

- The origin of diffuse hot gas in the spiral galaxies.
- Relation of the diffuse hot gas with H I .

Origin of the diffuse gas :

Our sample is made up of 34 spiral galaxies, of which 31 galaxies have the Infrared Astronomy Satellite (IRAS) observation and therefore available values for FIR fluxes and all

34 galaxies have 2 Micron All Sky Survey (2MASS) observations for K-band magnitudes. Thus with an advantage of a larger sample than the previous two studies, in the present study we revisit this problem to see if the mass or the star formation of a galaxy decides its X-ray gas content. Fig 6 shows the plot of diffuse Xray luminosity in 0.3 to 2 keV (L_X) vs K-band luminosity(L_K). Here L_K has been estimated from the 2MASS K-band magnitude values listed in NASA/IPAC Extragalactic Database (NED) (eqn. 6)(data from : Two Micron All Sky Survey Team, 2003, 2MASS Extended Objects. Final Release, The 2MASS Large Galaxy Atlas [74]). Fig 7 shows the plot of L_X vs far infra-red luminosity estimated from IRAS 60 and 100 micron data (L_{FIR}) (data from: ([131], [118], [121], "The Faint Source Catalog, version 2.0, Moshir et al. 1990).). L_K and L_{FIR} have been estimated using eqn. 6 and 4 respectively where, $S_{60_{\mu m}}$ and $S_{100_{\mu m}}$ are the IRAS 60 and 100 micron flux in Jy, D is the distance to the galaxy in Mpc, $L_\odot$ is solar bolometric luminosity, M_K is K-band absolute magnitude from 2MASS, and $M_\odot$ is the absolute magnitude of the Sun. Table 4 lists the estimated K-band luminosities, FIR luminosities and SFRs for these galaxies.

$$M_\odot - M_K = 2.5log(L_K/L_\odot) \tag{5.6}$$

Star formation rates in these galaxies were calculated using eqn. 5, from the FIR luminosities. In Fig. 6 normal galaxies (defined here as galaxies with star formation rate (SFR) < 1 $M_\odot$ yr^{-1}) are represented by empty circles, and starbursts (defined here as galaxies with SFR $\geq$ 1 $M_\odot$ yr^{-1}) by filled circles. Spearman rank correlation coefficient for the entire data returned a value of 0.46, with a probability (p) of 0.054 that they are uncorrelated. A visual inspection of the plot showed starbursts to posses more diffuse gas compared to normals of similar size and normal galaxies to be better correlated than the starbursts. Correlation coefficient for normals was a strong 0.72 with the p=0.003, while the same for starbursts was 0.19 with p=0.474.

In Fig 7, filled circles represent starburts and empty circles represent normal galaxies. Here starbursts look better correlated than normals. Correlation coefficient for the entire sample

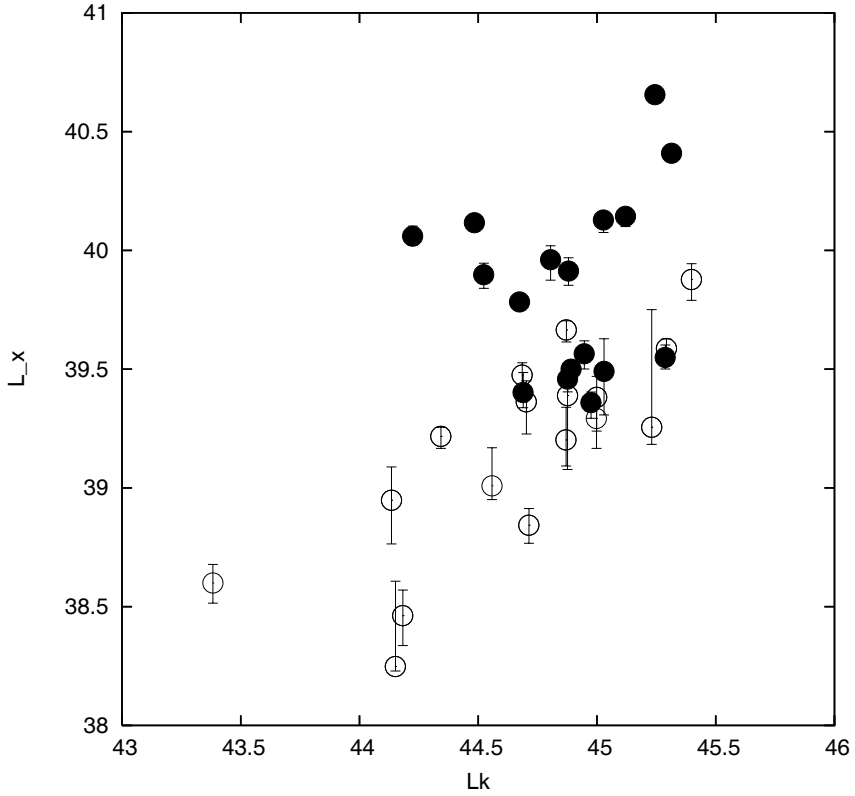

Figure 5.6: L_X against L_K, both plotted in log scale

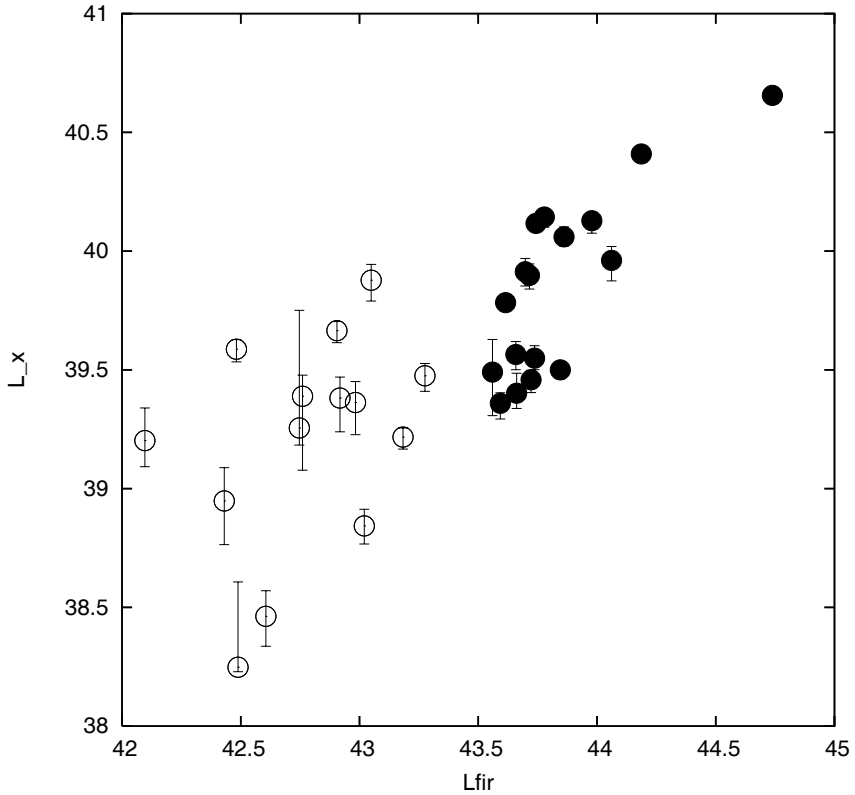

Figure 5.7: L_X against L_{FIR}, both plotted in log scale

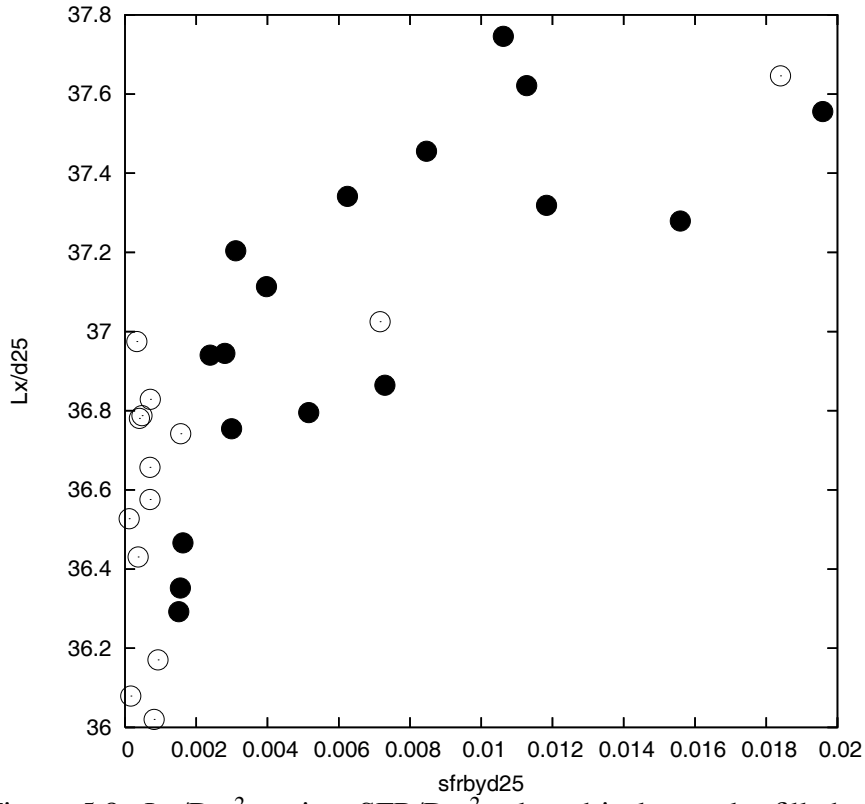

Figure 5.8: $L_X/D_{25}{}^2$ against $SFR/D_{25}{}^2$, plotted in log scale, filled circles are for SFR $\geq$ 1 $M\odot yr^{-1}$

was 0.78 with $p < 0.0001$. Starbursts separately yielded a correlation coefficient of 0.76 with $p < 0.0001$, and the same for normals was 0.375, with p=0.185.

Fig 8 shows a plot of X-ray surface brightness ($L_X/D_{25}{}^2$) vs star formation per unit disk area ($SFR/D_{25}{}^2$), where D_{25} is in kpc. While Strickland et al, 2004 [138], reported a good correlation with mostly starbursts in their sample (their x-axis being $f_{FIR}/D_{25}{}^2$, 'f' denoting flux) , we see a good correlation in the higher SFR side, where the starbursts are expected. Towards the end of low SFR per unit disk area, the correlation with L_X seems to become weaker. The correlation coefficient of this set of data with all the galaxies is 0.77, with a $p < 0.0001$. With only the starbursts the correlation coefficient improves to 0.82 with $p < 0.0001$.

H I and the diffuse X-ray gas :

Section 1.1.2 mentions the previous studies carried out on the correlation of star formation in the disk and its H I content. Since star formation rate is linked to the FIR luminosity, and the diffuse X-ray luminosity has been seen to correlate very well the FIR luminosity, it is interesting to study how the H I content of the galaxy is related with the diffuse X-ray luminosity. All these galaxies had existing single dish H I observations in the literature. We have acquired the integrated flux density values of the galaxies from literature using 'A general Catalog of H I observations of galaxies' [68]. The estimates of the H I mass, H I surface densities and H I deficiencies (described below in detail) for all the galaxies, are listed in table 4.

Fig 9, is a plot of H I surface density versus $L_{FIR}/D_{25}{}^2$ (a measure of FIR luminosity per unit area of the disk). There seems to be a correlation between, H I mass per unit area to FIR luminosity per unit area, which is an indirect form of the Schmidt law mentioned above, as SFR is estimated from the FIR luminosity. The correlation coefficient is 0.39, with a probability of p=0.029. Several observations have verified directly or indirectly the relation of cold gas and star formation as given by the Schmidt law. One of the recent studies, with a huge sample of about 1000 nearby (z$\sim$ 0) galaxies showed the H I mass to be related with the SFR of the galaxy by the relation given by eqn. 2, a relation which has been verified for higher redshift galaxies as well [41], [86]. In Fig 10 we have plotted H I mass against SFR (in log scale) and the straight line is not a fit to the data but represents eqn. 2. Correlation coefficient of this plot is 0.45 with p=0.01.

H I deficiency of a galaxy is a measure of its H I content when compared with the average H I content of an isolated galaxy of the same size and morphological type. By definition it is

$$\mathrm{def_{H_I}} = \log \frac{M_{H_I}}{D_l^2}|_{field} \; - \; \log \frac{M_{H_I}}{D_l^2}|_{obs} \tag{5.7}$$

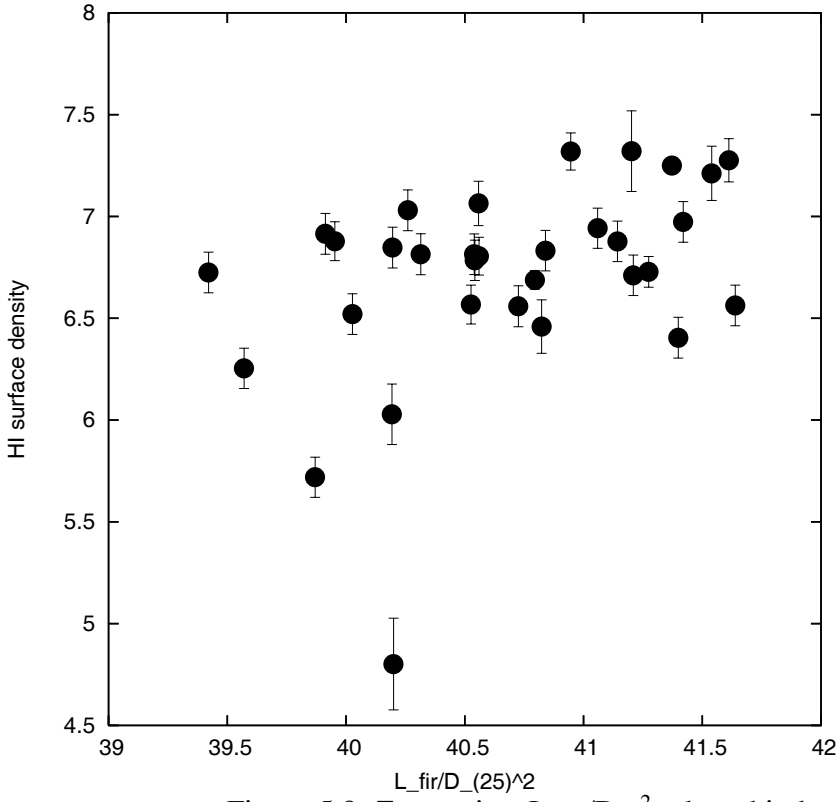

Figure 5.9: $\Sigma_{H\,i}$ against $L_{FIR}/D_{25}{}^2$, plotted in log scale

where M_{H_l} in the second term of right hand side of the equation, is the total observed H I mass of a galaxy and D_l is the optical major isophotal diameter (in kpc) measured at or reduced to a surface brightness level m_B = 25.0 mag/arcsec^2.

The expected field values of $M_{\rm H_I}/D_l^2$ for various morphological types are taken from [59]. While the authors [59] used the UGC blue major diameters for D_l, in this work RC3 major diameters have been used. To take care of the difference in the surface matter densities that result from the use of RC3 diameters, a value of 0.08 [51] has been added to the expected surface matter densities given by Haynes & Giovanelli (1984)[59].

Fig. 11 shows H I deficiency plotted against log(L_X/L_K). H I deficiency shows a decreasing trend with increasing X-ray luminosity per unit mass. The correlation coefficient is -0.26, with a probability of 0.127.

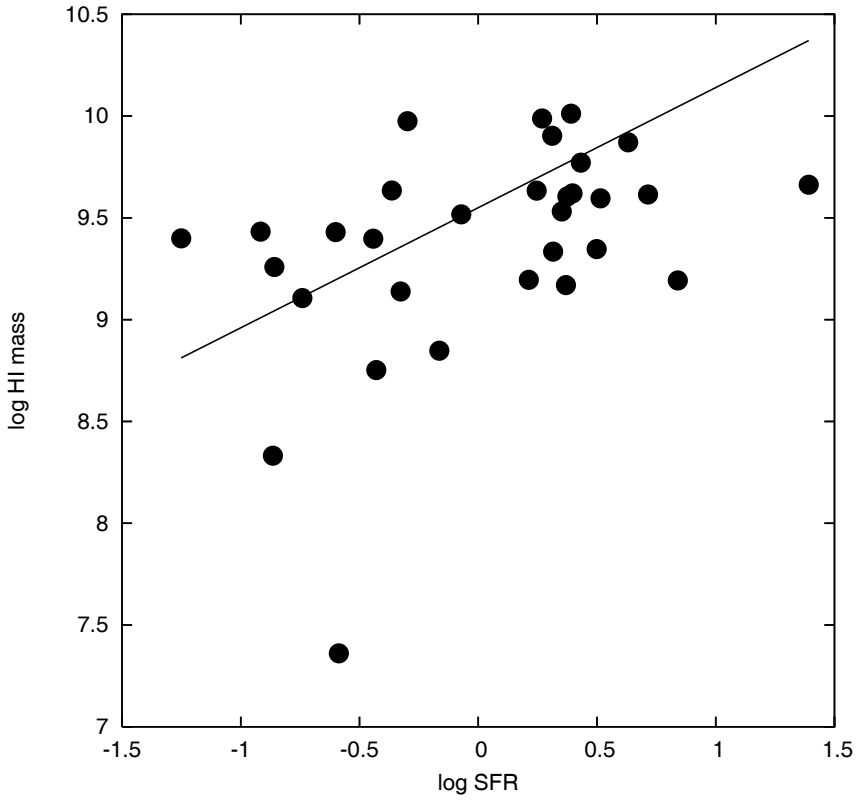

Figure 5.10: H I mass against SFR in log scale, the straight line is the relation of H I mass and SFR in z ∼0 universe given in eqn. 2 (ref. Lah et al 2007)

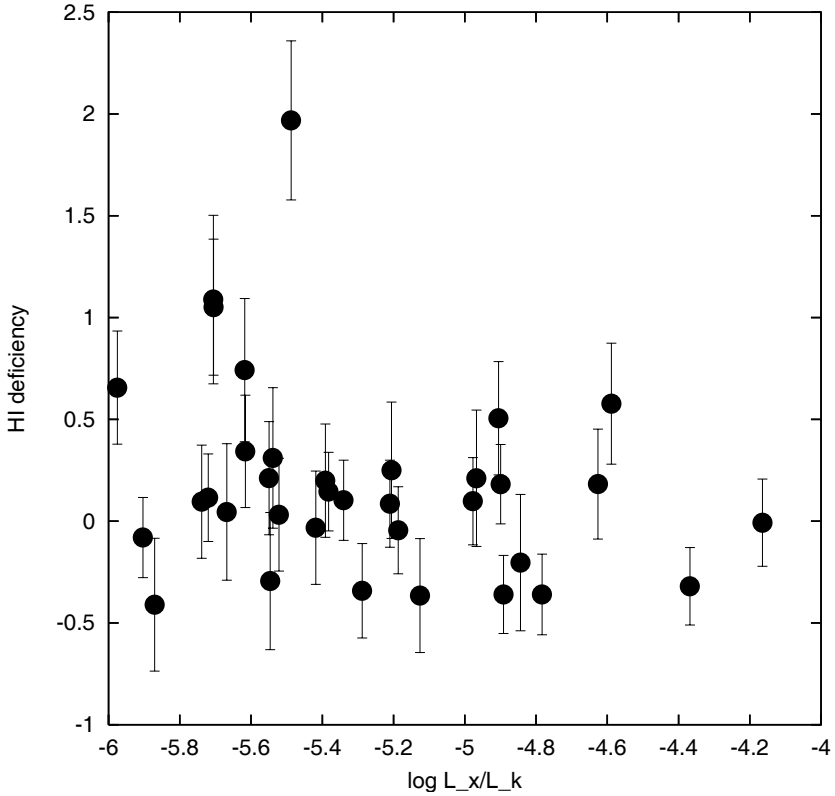

Figure 5.11: H I deficiency against $\log(L_X/L_K)$ for the entire sample

Normal galaxies and galaxies with AGN: The correlation of H I deficiency versus diffuse X-ray luminosity seems to be weak when all the galaxies are plotted together. However, if galaxies without and with AGN's are plotted separately, we get the following results. Fig 12 to Fig 15 show the plots of H I deficiency versus $\log(L_X/L_K)$, for galaxies without and with AGN. The straight lines plotted in Fig. 12 and Fig. 14, mark the zero H I deficiency level. Two points need to be noticed in Figs. 12 and 14. Firstly, on an average, the subsample of AGN hosts have more galaxies above the H I deficiency=0 line, than the one without AGN hosts. The large errorbars along the y axis hinders any study of H I deficiency for single galaxies. But on an average the galaxies in Fig 14 seem to lie above the zero line. Secondly, the galaxies without AGNs show a trend of decreasing H I deficiency with increasing X-ray luminosity per unit mass. For the AGN hosts, this doesn't seem to happen. At higher values of X-ray luminosity, there seem to be extra H I deficiency, compared to the non AGN host galaxies. The correlation coefficient for the galaxies without AGN is -0.46, with a probability of 7.5%, compared to the AGN hosts, where the correlation coefficient is 0.28, with a probability of 25.7%. Straight line fits to the data shows a change in the sign of the slope for galaxies with and without AGNs. For the former the slope is -0.35 ± 0.12, which changes to 0.09 ± 0.15 for the AGN hosts. Table 5 lists the slope and intercept values to the liner fits and the Spearman rank correlation coefficient values with respective probabilities for all the plots used in this work.

5.4 Discussion

Two major studies have till date attempted to explore the relation between the properties of the hot diffuse IGM in spiral galaxies to other measurable properties relating to the mass and star formation, as well as their environment. The first ever work carried out to study the multiwavelength behaviour of the hot gas in spirals, was that of Read & Ponman (2001). With a sample of 17 galaxies, observed with ROSAT, the authors studied the origin of the

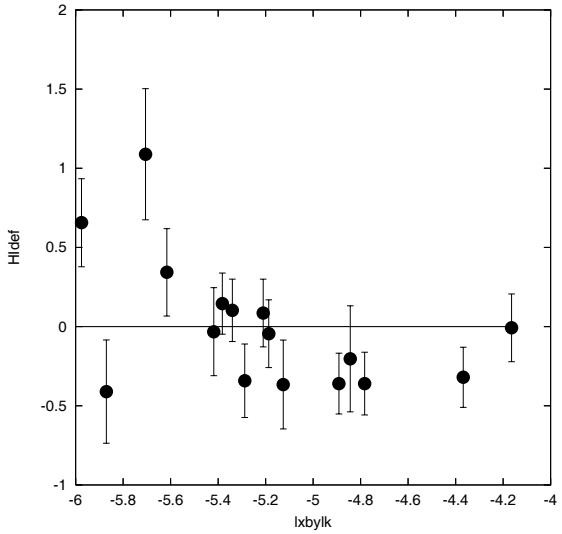

Figure 5.12: H I deficiency against $\log(L_X/L_K)$ in normal galaxies, the straight line indicates 0 deficiency

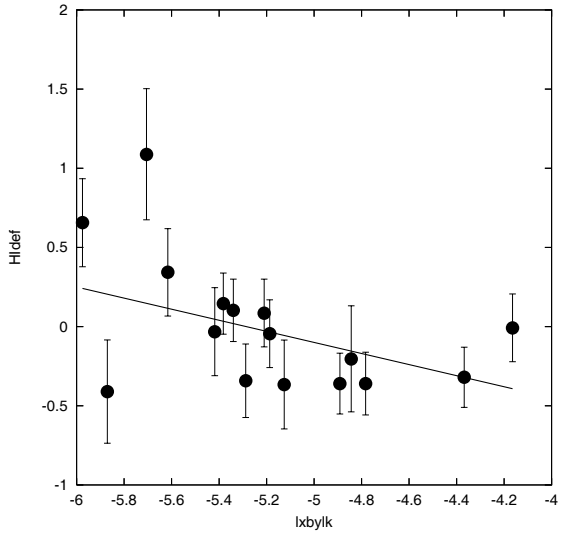

Figure 5.13: H I deficiency against $\log(L_X/L_K)$ in normal galaxies, the straight line is a fit to the data

hot gas in spirals. The second work was with 10 spirals, mostly starbursts, observed with Chandra, which explored the origin of the hot gas, its relation to star formation in the galaxy and the quantified the efficiency of supernovae related of the ISM.

However, for reasons described below, the problem of the origin of hot gas in spirals needed to be revisited. Our present study was important and timely because of the following reasons,

- ROSAT data suffered from lack of proper point source removal- This is a very crucial aspect of studying the diffuse gas in galaxies. With the resolution of ROSAT, it was nearly impossible to detect and remove point sources properly. Presence of point sources, especially the HMXBs can contribute to large error in the diffuse flux estimates and therefore the high spatial resolution of Chandra makes it the ideal instrument to study this hot gas in galaxies.

- Work carried out with the Chandra data had only 10 galaxies and of them 7 were starbursts, making the study biased towards starburst galaxies. This study only could concentrate on the origin of the hot gas in starburst galaxies, but failed to confirm some of the comparative results of Read & Ponman (2001), estimated for normal and starburst galaxies with the ROSAT data. Also as a statistical study for only starburst

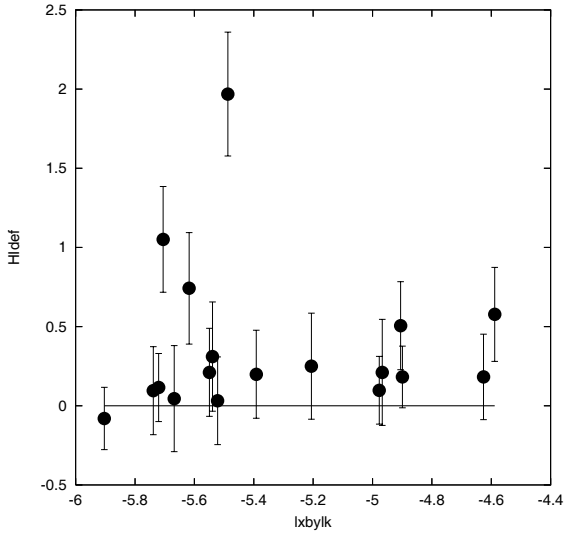

Figure 5.14: H I deficiency against $\log(L_X/L_K)$ in AGN hosts, the straight line indicates 0 deficiency

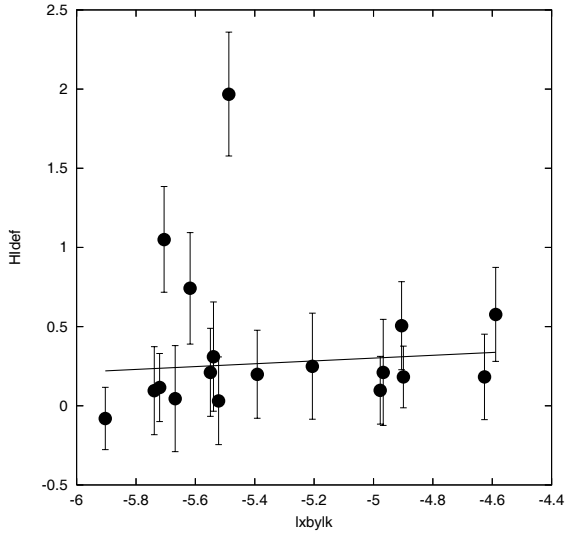

Figure 5.15: H I deficiency against $\log(L_X/L_K)$ in AGN hosts, the straight line is a fit to the data

galaxies, this work was very detailed and exhaustive but was based on a very small number of galaxies: 7 starbursts.

- Relation of cold gas (H I) and hot gas (X-ray emitting) was never explored before. Because there were suggestions from the previous two studies that the hot gas is related to the SFR of the galaxy, at least for the higher star forming galaxies, and at the same time Schmidt law was observationally proved to be valid for H I and star formation rate in spirals, it was interesting to study the relation of the hot gas and H I in these galaxies.

- Unresolved point source contribution was subtracted from the modeled flux values to get a correct estimate of the diffuse flux. Even with the high resolution of the Chandra, there remained unresolved point source contamination in the estimates of the diffuse fluxes. This contribution can be, in some cases 15% to 20% of the total diffuse flux. Thus it was important to take care of this issue while estimating the diffuse flux values.

So with a bigger sample than any previous similar study, making use of the highest spatial resolution available, we carried out a quantitative, multiwavelength comparative study of the

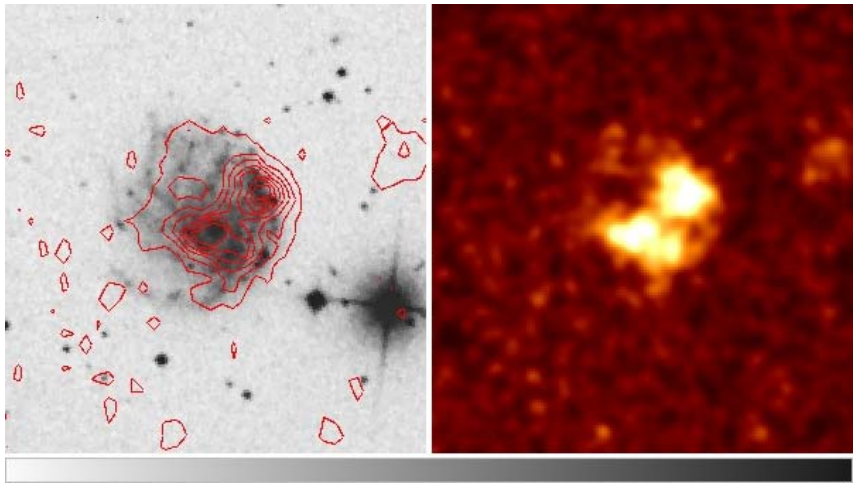

Figure 5.16: High resolution, 0.3-2.0 keV X-ray images of NGC 2276:left- Xray contours overlayed on optical image, right- X-rays in colour

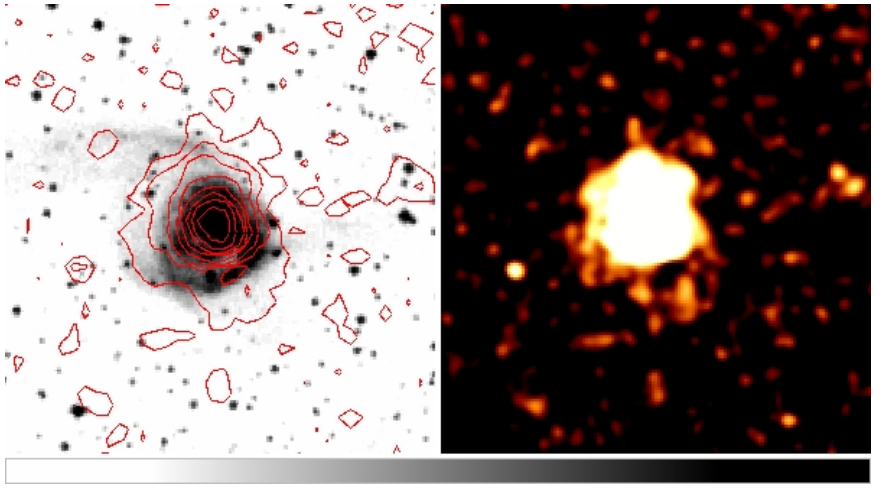

Figure 5.17: High resolution, 0.3-2.0 keV X-ray images of NGC 3256:left- Xray contours overlayed on optical image, right- X-rays in colour

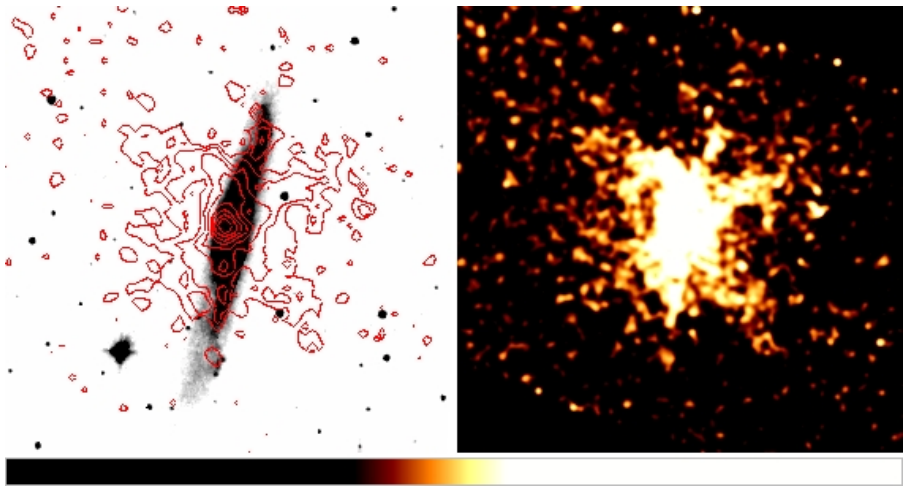

Figure 5.18: High resolution, 0.3-2.0 keV X-ray images of NGC 3079:left- Xray contours overlayed on optical image, right- X-rays in colour

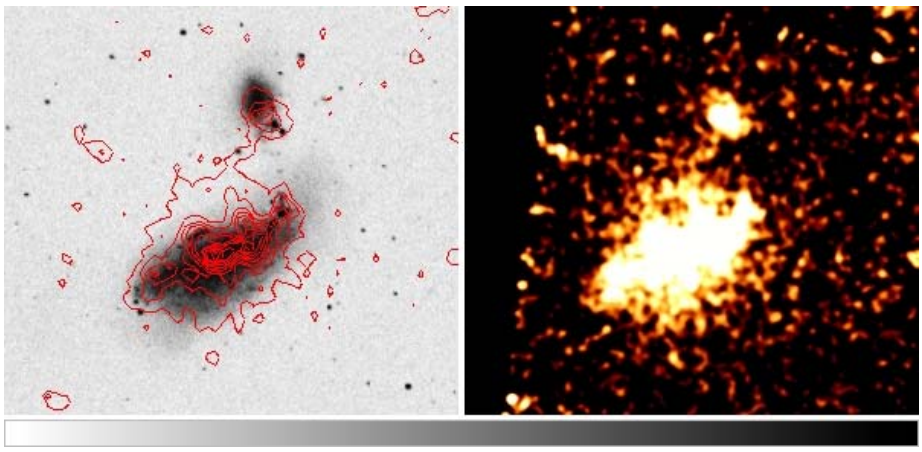

Figure 5.19: High resolution, 0.3-2.0 keV X-ray images of NGC 4485 and NGC 4490:left- Xray contours overlayed on optical image, right- X-rays in colour

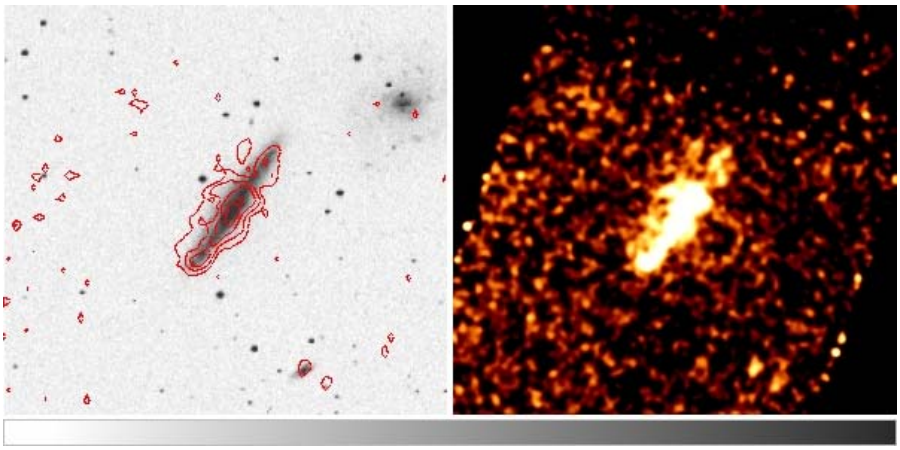

Figure 5.20: High resolution, 0.3-2.0 keV X-ray images of NGC 5775:left- Xray contours overlayed on optical image, right- X-rays in colour

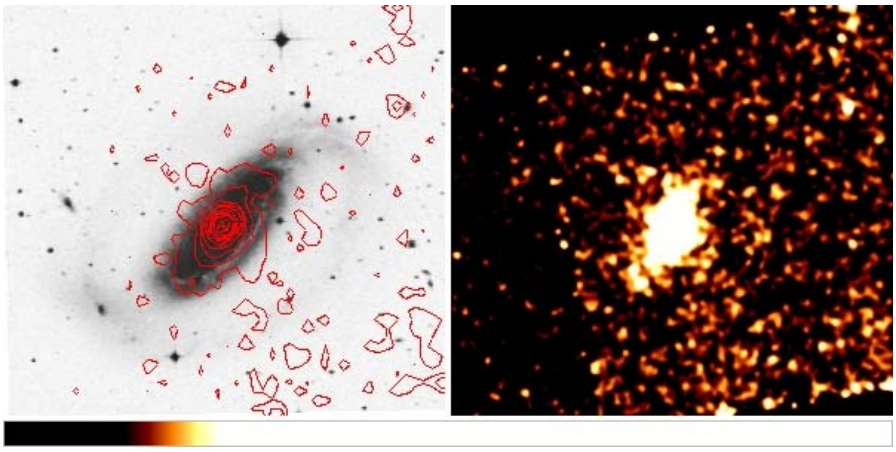

Figure 5.21: High resolution, 0.3-2.0 keV X-ray images of NGC 1808:left- Xray contours overlayed on optical image, right- X-rays in colour

properties of the hot gas.

Origin of hot gas in spirals : Read & Ponman (2001), studied the correlation of diffuse X-ray luminosity (L_X) with FIR luminosity (L_{FIR}) and B band luminosity (L_B), in order to study the source of the hot gas in spiral galaxies. They defined L_B as 'mass' as this traces the stellar matter of the galaxy and L_{FIR}/L_B as 'activity' as it is a measure of SFR per unit mass.

The authors compared the X-ray emission with the galaxy mass for the total sample as well as for the normal and starburst subsamples separately. In the normal galaxy subsample, in the low X-ray emission regime, diffuse luminosity had a tight correlation coefficient of 0.95 with 'mass', which worsens to 0.49 when applied to the entire sample. For the normal galaxies, this result suggested that large galaxies are able to heat or retain a larger fraction of their gas than smaller galaxies, or they compress it to higher mean densities. One plausible picture is that hot gas from active star formation regions is able to escape more readily from the shallower potential wells of small galaxies, systematically lowering their hot gas fraction. However correlation studies of L_X and L_{FIR}, yielded a value of 0.80 for the entire sample, and a better 0.86 for the starburst subsample. Thus it seemed activity was an important property for both normals and starbursts and no significant change was seen between the normal and the starburst galaxies, though effect of mass (L_B) was insignificant in determining the X-ray emission in the starburst galaxies.

In the case of starburst galaxies, the fraction of diffuse emission (i.e. hot gas) was primarily determined by activity rather than galaxy mass, which was reflected by the poorer correlation coefficient of 0.49 in L_X vs L_B plot and the strong correlation coefficient of 0.86 for the L_X vs L_{FIR} plot. This suggests that the influence of the galaxy potential, important for the normal galaxies above, is no longer as important. The activity now dominates, having reached such a level that whether the galactic potential is large or small has little effect. Thus the broad outcome of these correlation studies was that starbursts in general, have high activity and also higher diffuse X-ray emission than normal galaxies. Also normal galaxies appear to be very much more influenced by their mass than by their activity. For starburst galaxies, on the

other hand, it is activity that is the dominating factor.

With our sample of 34 spiral galaxies, we carried out the similar correlation tests of L_X with FIR luminosity (L_{FIR}) and K band luminosity (L_K). Read & Ponman (2001) used optical luminosity, L_B, as their measure of mass. However, they note that this was not ideal, because the blue luminosity to mass ratio is quite sensitive to the age of a stellar population and that luminosity in the near-infrared would be a more robust indicator of stellar mass. As most of the galaxies in their sample did not have IR data, they had to use optical B band data as a measure of mass. For our sample we have used the 2MASS K band data as a measure of mass.

Correlation coefficient for L_X and L_K for the entire sample is 0.46, which is similar to the result of Read & Ponman (2001) [116], suggesting an overall correlation between the hot gas and the mass of the galaxies. However the results of the correlation study of normal and starburst subsample (all galaxies which have SFR ≥ 1 $M_\odot$ yr^{-1} were included in the starburst sample), reveal a marked difference in their behaviour. While the correlation coefficient for the normals is 0.72, the same for the starbursts turns out to be 0.19, as compared to 0.95 and 0.66 from Read & Ponman (2001) for the two subsamples respectively and confirms their conclusions. The starbursts are consistently seen to have higher X-ray luminosities compared to a normal galaxy of similar 'mass'. But the normals are better correlated in terms of L_X and L_K than starbursts, suggesting 'mass' has a bigger role to play in the X-ray emission in normals compared to starburts.

X-rays seem to correlate very well with the FIR emission, for our entire sample. The correlation coefficient is 0.78 compared to 0.80 in Read & Ponman (2001). For normals and starbursts separately the coefficients are 0.38 and 0.76 respectively, compared to 0.63 and 0.86 in Read & Ponman (2001). One important feature of the plot of L_X and L_{FIR} is the clear division of starburst and normals towards the higher L_X side. Starbursts tend to have higher X-ray emission than the normal galaxies. When divided into normal and starburst subsamples, the galaxies behave just the reverse of L_X vs L_K plots. Correlation coefficient for the

starburst sample is 0.76 and that of normals is 0.38 compared to 0.86 and 0.63 from Read & Ponman (2001). The fact that starbursts are better correlated with star formation activity can also be supported by the our Fig. 8. X-ray luminosity per unit area of galaxies with SFR ≥ 1 $M_\odot$ yr^{-1}, show a better correlation with SFR per unit area of the disk, as was also found by Strickland et al (2004) [138].

The overall consistency in the correlation in the L_X and L_{FIR} plot, suggests star formation to be the origin for X-ray gas in spirals. The fact that there is a weak correlation for galaxies with SFR < 1 $M_\odot$ yr^{-1}, that are assumed to be not undergoing an intense star formation recently, suggests that current star formation is not the only factor contributing to the diffuse X-ray flux. The presence of X-rays in normal subsample can be contributed by the current star formation as well as past bursts of star formation. The strong correlation of the hot gas with mass in this subsample supports the idea that this hot gas, which can be mostly heated by past star formations in the disk, is held back to the galaxy by the virtue of its 'mass'. Higher the mass, deeper is the galaxy potential and hence it is able to hold on to its hot gas mass better.

Cold gas and hot gas in spirals : Cold gas and star formation in a galaxy are related by the Schmidt law (see eqn. 1). Several observations have verified it directly or indirectly. Since X-rays in spiral galaxies are closely related to the star formation rates in the galaxies, it becomes interesting to study the relation of cold gas and the X-ray emitting hot gas in these spirals. A recent work by Doyle & Drinkwater (2006), carried out with a huge sample of galaxies, concluded that a strong correlation exists between the HI mass and SFR for these galaxies. The two quantities were found to be related by eqn. 2. In a subsequent work, this relation was verified by Lah et al for galaxies at a higher redshift ($z \sim 0.2$).

Our sample of ~ 30 galaxies also verify the above correlation. Our results suggest that there exists a correlation of H I mass and SFR in a galaxy, the modest correlation coefficient can be an effect of using 30 galaxies, in comparison with the results of a sample of ~ 1000 galaxies. Because of the small number of galaxies, some more plots like Σ_{HI} vs $\log(L_{FIR}/L_K)$, Σ_{HI} vs

$\log(L_{FIR}/{D_{25}}^2)$ were studied, to check the correlation from different angles. The correlation coefficients indicate that a modest correlation exists between the SFR and cold gas in these galaxies, which is an indirect confirmation of the Schmidt law.

Since X-ray and FIR luminosities in these galaxies are closely correlated, the next obvious thing to expect was a X-ray and H I correlation. In fact one of the main motivations of this work was to study the relation between X-ray luminosity and H I content of the galaxies. In Chapter 2 and 3 of this thesis, we have discussed about how the hot X-ray emitting intra-group medium (IGM) assists in stripping H I from the galaxies, making them gas deficient. As a continuation of studying the relation of hot and cold gas, we undertook this project of studying the H I in X-ray bright spiral galaxies. The idea was to see if the H I content of a galaxy is altered or influenced by the X-ray emitting gas and vice-versa.

To study the relation of hot gas and H I in these galaxies, we studied the correlation of L_X and H I deficiency for the sample. With the entire sample, the plot of H I deficiency against X-ray luminosity per unit mass, yields a correlation coefficient of -0.26. Visually, the plot shows a faint indication that H I deficiency is high for galaxies with lower L_X/L_K. The H I deficiency attains a flat distribution as the L_X/L_K increases, with almost equal number of galaxies on either side of the zero H I deficiency line. Though low in terms of probability, but this trend suggests that the H I deficiency can actually be the reason of less star formation, and thereby lower X-ray per unit mass in these galaxies. This can be indirectly interpreted as a supporting evidence in favour of the Schmidt law.

There is a striking change in the behaviour of H I deficiency and X-ray luminosity in these galaxies when we divide the sample into galaxies with and without AGN hosts. First difference to be noted between the two subsamples is the increase in the average deficiency in the AGN hosts. Number of galaxies above the zero H I deficiency line in the Figs 12 and 14, is higher for the AGN hosts than in normals, especially on the higher L_X/L_K side. This implies that towards the higher L_X/L_K side amongst the AGN hosts, galaxies are in some way losing

more gas than the galaxies which do not host an AGN.

The second difference is the change of the slope of the fit to the data from negative in galaxies without AGN to positive in galaxies with an AGN. A straight line fit to the subsample (H I deficiency vs L_X/L_K) of galaxies without AGNs, yields a slope of -0.35 ± 0.12 and a correlation coefficient of -0.45, stating H I deficiency in these galaxies decrease as L_X/L_K increase. This result is consistent with the basic idea of the Schmidt law, that higher star forming galaxies must have higher supplies of cold gas. However, for the galaxies which host AGNs, the straight line fit to the data (H I deficiency vs L_X/L_K), has a positive slope of 0.089 ± 0.152, which is consistent with zero within the errorbars. The correlation coefficient value is 0.28, which suggests an increasing H I deficiency with L_X/L_K. So this subsample deviates from the usual trend expected from the Schmidt law, and for higher star forming galaxies especially, there seems to be an excess H I deficiency over what was already existing in the galaxy.

With the present available information it is difficult to make any strong statement about what created H I deficiency in these galaxies, in both the subsamples of galaxies with and without AGNs. A past event has probably created the H I deficiency in the sample galaxies. Since FIR traces the current star formation, the results we get suggests that the star formation and thereby the hot diffuse gas is being affected by the lack of cold gas (H I deficiency). At least for the set of galaxies without AGNs this seems to be a logical way to explain the results. But for AGN hosts, we notice an increase in H I deficiency compared to the non AGN host galaxies. For a certain value of L_X/L_K, we notice the AGN host galaxy will have a higher H I deficiency than a non AGN host galaxy. A possible explanation can be that this excess deficiency is induced by a recent merger or interaction, processes which are capable of pulling out large quantities of gas from the galaxies and at the same time, can increase star formation activity in the galaxy. Therefore we see higher star formation and higher X-ray emission as well as higher values of H I deficiency in these galaxies, preferably at the higher L_X/L_K side of the AGN host subsample.

It is not impossible to have these galaxies in the non AGN subsample. But several previous

studies have shown the connection of merger/interaction related AGN activity in galaxies [161], [3]. These studies show that the probability of an AGN to occur in a interacting galaxy system is higher than in non-interacting systems. This might explain why we see the positive correlation in the AGN host subsample only. So these interactions can trigger AGN activity, star formation and at the same time can also remove gas from the galaxies leaving them H I deficient.

Available interaction histories of some of these galaxies from the literature can help to explain the phenomenon better. In this subsample, some of the galaxies with high H I deficiency as well as high value of L_X/L_K, have been known to be either merger or interacting galaxies. Figs 12 and 14 show that in galaxies without AGN, the H I deficiency consistently falls with increasing X-ray luminosity per unit mass and the L_X/L_K value where the H I deficiencies fall below the zero deficiency line is roughly -5.6. We will concentrate on histories of galaxies with AGN which have $L_X/L_K \geq$ -5.6. NGC 3256 is a well known merger induced starburst galaxy, NGC 7714 is interacting with another spiral NGC 7715, and H I observations show massive bridge connecting the two galaxies. NGC 1068, hosting a bright AGN is known to have warped disks, which can be a result a interaction, NGC 1808 is a tidal induced starburst galaxy, NGC 2782 is a merger remnant and is seen to have H I tidal tails, NGC3079 is known to have an interaction, NGC 5728 is a remnant of a minor merger and NGC 3190 has had a recent tidal interaction. However, it is important to note at this point that this phenomenon is not unique to only AGN hosts and is possible for non AGN host galaxies also. But it is the higher probability of association of AGN with interacting galaxies where higher H I deficiency is expected, that probably makes AGN hosts have H I deficient galaxies at higher L_X/L_K, in contrast to what is normally expected from the Schmidt law.

5.5 Conclusion

The main conclusions that came out of this quantitative comparative study of the X-ray emitting gas in a sample of 34, Chandra observed, spiral galaxies are the following

- In galaxies, with SFR $\geq$ 1 $M_{\odot}$ yr^{-1}, the X-ray emission is tightly correlated with the FIR emission, suggesting the star formation in the galaxy to be the main contributor to the X-ray emission.

- In galaxies, with SFR $<$ 1 $M_{\odot}$ yr^{-1}, the X-ray emission is better correlated with the mass of the galaxy than its SFR, suggesting the mass to be main deciding factor for the hot gas content of the galaxy.

- On an average, galaxies with higher H I deficiency show lower hot gas content– an indirect confirmation of the Schmidt law.

- However, the subsample of AGN host galaxies, show marginal increase in H I deficiency with increasing X-ray luminosity–higher probability of interacting /merger galaxies to be AGN hosts can be a possible explanation.

Table 5.1: Sample Properties

Name	Coordinate J2000	V_{opt} kms^{-1}	Distance Mpc	d_l (')	M type	Comment
NGC278	00 52 04.3 +47 33 02	627	10.0	2.1	Sb	N
NGC891	02 22 33.4 +42 20 57	528	8.7	13.5	Sb	N
NGC1068	02 42 40.7 -00 00 48	1137	12.0	7.1	Sb	A
NGC1808	05 07 42.3 -37 30 47	995	11.0	6.5	Sb	A
NGC2146	06 18 37.7 +78 21 25	893	12.0	6.0	Sab pec	N
NGC2276	07 27 14.3 +85 45 16	2410	28.1	2.8	Sc	N
NGC2782	09 14 05.1 +40 06 49	2543	30.1	3.5	Sa	A
NGC2841	09 22 02.6 +50 58 35	638	15.0	8.1	Sb	A
NGC3079	10 01 57.8 +55 40 47	1116	17.0	7.9	Sc	A
NGC3184	10 18 17.0 +41 25 28	592	11.5	7.4	Scd	N
NGC3190	10 18 05.6 +21 49 55	1271	18.0	4.4	Sa pec	A
NGC3256	10 27 51.3 -43 54 14	2804	32.1	3.8	Pec	A
NGC3310	10 38 45.9 +53 30 12	993	17.0	3.1	Sbc	N
NGC3351	10 43 57.7 +11 42 14	778	9.0	3.1	Sb	N
NGC3507	11 03 25.4 +18 08 07	979	16.6	3.4	Sb	A
NGC3556	11 11 31.0 +55 40 27	699	14.0	8.7	Scd	N
NGC3631	11 21 02.8 +53 10 11	1156	16.0	5.0	Sc	N
NGC3683	11 27 31.8 +56 52 37	1716	22.0	1.8	Sc	N
NGC3898	11 49 15.4 +56 05 04	1176	17.0	4.4	Sab	A
NGC4136	12 09 17.7 +29 55 39	609	15.6	4.0	Sc	N
NGC4151	12 10 32.6 +39 24 21	995	15.0	6.3	Sab	A
NGC4303	12 21 54.9 +04 28 25	1566	15.6	6.5	Sbc	A
NGC4314	12 22 32.0 +29 53 43	963	15.6	4.2	Sa	A
NGC4485	12 30 31.1 +41 42 04	493	11.8	2.3	Im pec	N
NGC4490	12 30 36.4 +41 38 37	565	11.8	6.3	Sd pec	N
NGC4594	12 39 59.4 -11 37 23	1024	8.0	8.7	Sa	A
NGC5728	14 42 23.9 -17 15 11	2804	25.9	3.1	Sa	A
NGC5746	14 44 55.9 +01 57 18	1724	18.0	7.4	Sb	N
NGC5775	14 53 57.6 +03 32 40	1681	18.0	4.16	Sb	N
NGC5879	15 09 46.8 +57 00 01	772	13.0	3.7	Sbc	A
NGC6503	17 49 26.5 +70 08 40	60	6.3	7.1	Scd	A
NGC7331	22 37 04.1 +34 24 56	816	13.0	10.5	Sb	A
NGC7714	23 36 14.1 +02 09 19	2798	30.1	1.9	Sb pec	A
NGC7727	23 39 53.9 -12 17 35	1868	20.0	4.7	Sa pec	N

Table 5.2: Observation Details

Name	Obs Id	Date of Obs	exposure time (ks)	Detector	Data Mode
NGC278	2055	2001-06-22	38.75	ACIS-S	FAINT
NGC891	794	2000-11-01	51.56	ACIS-S	VFAINT
NGC1068	344	2000-02-21	48.05	ACIS-S	FAINT
NGC1808	3012	2002-12-19	43.43	ACIS-S	FAINT
NGC2146	3135	2002-11-16	10.15	ACIS-S	FAINT
NGC2276	4968	2004-06-23	46.17	ACIS-S	VFAINT
NGC2782	3014	2002-05-17	29.96	ACIS-S	FAINT
NGC2841	6096	2004-12-18	28.58	ACIS-S	VFAINT
NGC3079	2038	2001-03-07	26.92	ACIS-S	FAINT
NGC3184	1520	2000-02-03	24.04	ACIS-S	FAINT
NGC3190	2760	2002-03-14	20.07	ACIS-S	FAINT
NGC3256	3569	2003-05-23	27.58	ACIS-S	VFAINT
NGC3310	2939	2003-01-25	48.23	ACIS-S	FAINT
NGC3351	5929	2005-02-08	39.96	ACIS-S	FAINT
NGC3507	3149	2002-03-08	39.76	ACIS-S	FAINT
NGC3556	2025	2001-09-08	60.12	ACIS-S	FAINT
NGC3631	3951	2003-07-05	90.21	ACIS-S	VFAINT
NGC3683	4659	2004-04-07	40.17	ACIS-S	VFAINT
NGC3898	4740	2005-02-10	58.18	ACIS-S	VFAINT
NGC4136	2921	2002-06-08	19.96	ACIS-S	FAINT
NGC4151	348	2000-03-07	27.95	ACIS-S	FAINT
NGC4303	2149	2001-08-07	28.38	ACIS-S	FAINT
NGC4314	2062	2001-04-02	16.28	ACIS-S	FAINT
NGC4485	4725	2004-07-29	38.96	ACIS-S	VFAINT
NGC4490	4725	2004-07-29	38.96	ACIS-S	VFAINT
NGC4594	1586	2001-05-31	18.75	ACIS-S	FAINT
NGC5728	4077	2003-06-27	18.97	ACIS-S	FAINT
NGC5746	3929	2003-04-11	37.29	ACIS-I	VFAINT
NGC5775	2940	2002-04-05	58.96	ACIS-S	FAINT
NGC5879	2241	2001-06-10	90.1	ACIS-S	FAINT
NGC6503	872	2000-03-23	13.36	ACIS-S	FAINT
NGC7331	2198	2001-01-27	30.13	ACIS-S	FAINT
NGC7714	4800	2004-01-24	60.15	ACIS-S	FAINT
NGC7727	2045	2001-12-18	19.26	ACIS-S	FAINT

Table 5.3: Results

Name	X-radius (')	Xray centre	HMXB lum (erg/s)	L_{X-ray} ± error (erg/s)
NGC278	1.46	00 52 04.70 +47 33 04.02	38.04	$39.21^{0.05}_{0.03}$
NGC891	2.80	02 22 32.8 +42 20 57.75	38.04	$39.35^{0.06}_{0.04}$
NGC1068	2.32	02 42 41.0 -00 00 39.67	39.19	$40.40^{0.01}_{0.00}$
NGC1808	1.82	05 07 42.72 -37 30 52.18	38.77	$39.50^{0.03}_{0.02}$
NGC2146	3.90	06 18 41.26 +78 21 32.21	39.07	$39.96^{0.08}_{0.05}$
NGC2276	1.74	07 27 26.35 +85 45 17.63	38.69	$40.06^{0.03}_{0.04}$
NGC2782	1.49	09 14 04.7 +40 06 51.97	38.69	$39.91^{0.05}_{0.05}$
NGC2841	3.35	09 22 03.55 +50 58 51.38	37.80	$39.87^{0.08}_{0.06}$
NGC3079	3.47	10 01 58.9 +55 41 11.59	39.00	$40.12^{0.05}_{0.02}$
NGC3184	2.56	10 18 19.09 +41 25 23.73	37.86	$39.36^{0.13}_{0.08}$
NGC3190	1.48	10 18 06.29 +21 49 49.02	38.04	$39.38^{0.14}_{0.08}$
NGC3256	1.60	10 27 51.11 -43 54 07.81	40.11	$40.65^{0.02}_{0.02}$
NGC3310	1.86	10 38 47.21 +53 30 06.34	38.95	$40.11^{0.02}_{0.01}$
NGC3351	1.65	10 43 57.6 +11 42 19.59	37.89	$38.84^{0.07}_{0.06}$
NGC3507	1.49	11 03 25.06 +18 08 27.63	–	$39.00^{0.05}_{0.16}$
NGC3556	2.60	11 11 28.97 +55 40 15.48	38.27	$39.56^{0.06}_{0.05}$
NGC3631	2.24	11 21 02.04 +53 10 17.38	38.17	$39.47^{0.06}_{0.05}$
NGC3683	1.50	11 27 33.68 +56 53 08.67	38.63	$39.40^{0.06}_{0.08}$
NGC3898	1.67	11 49 15.88 +56 05 27.72	36.77	$39.20^{0.10}_{0.13}$
NGC4136	1.47	12 09 18.78 +29 56 36.94	37.30	$38.94^{0.18}_{0.14}$
NGC4151	1.49	12 10 32.65 +39 24 23.25	38.04	$39.66^{0.05}_{0.03}$
NGC4303	2.48	12 21 54.82 +04 29 01.72	38.76	$40.14^{0.04}_{0.03}$
NGC4314	1.58	12 22 31.57 +29 53 54.32	37.93	$39.38^{0.31}_{0.08}$
NGC4485	0.90	12 30 30.92 +41 41 45.85	–	$38.59^{0.08}_{0.07}$
NGC4490	2.31	12 30 35.49 +41 38 42.83	38.38	$39.78^{0.02}_{0.03}$
NGC4594	3.57	12 39 59.08 -11 37 23.68	37.04	$39.58^{0.05}_{0.04}$
NGC5728	1.53	14 42 24.03 -17 15 05.68	39.00	$39.49^{0.18}_{0.13}$
NGC5746	2.25	14 44 56.5 +01 58 28.70	37.43	$39.25^{0.07}_{0.49}$
NGC5775	1.76	14 53 57.6 +03 32 35.19	38.56	$39.45^{0.05}_{0.04}$
NGC5879	0.87	15 09 47.74 +57 00 04.34	37.25	$38.46^{0.12}_{0.10}$
NGC6503	2.25	17 49 26.98 +70 08 29.97	37.17	$38.24^{0.01}_{0.35}$
NGC7331	2.00	22 37 03.59 +34 25 00.66	38.56	$39.54^{0.04}_{0.05}$
NGC7714	1.30	23 36 13.46 +02 09 25.13	38.66	$39.89^{0.05}_{0.04}$
NGC7727	1.16	23 39 53.71 -12 17 40.37	–	$39.29^{0.12}_{0.06}$

Table 5.4: Results

Name	H I mass $M_\odot$	$\Sigma_{H\,i}$ ± error (in log)	H I deficiency ± error	L_K (log) (erg/s)	L_{FIR} (log) (erg/s)	SFR $M_\odot\ yr^{-1}$
NGC 278	8.84	7.27± 0.10	-0.36 ± 0.28	44.34	43.18	0.68
NGC 891	9.63	6.56± 0.09	0.34 ± 0.27	44.97	43.59	1.76
NGC 1068	9.19	6.40± 0.10	0.50 ± 0.27	45.31	44.18	6.92
NGC 1808	9.34	6.71± 0.09	0.19 ± 0.27	44.89	43.84	3.15
NGC 2146	9.61	6.97± 0.09	-0.20 ± 0.33	44.80	44.06	5.18
NGC 2276	9.59	6.87± 0.09	-0.00 ± 0.21	44.22	43.86	3.27
NGC 2782	9.53	6.55± 0.10	0.21 ± 0.33	44.87	43.69	2.24
NGC 2841	9.97	6.87± 0.09	0.03 ± 0.27	45.39	43.04	0.50
NGC 3079	9.87	6.68± 0.04	0.18 ± 0.19	45.02	43.97	4.27
NGC 3184	9.63	6.84± 0.10	0.10 ± 0.19	44.70	42.98	0.43
NGC 3190	8.75	6.02± 0.14	0.74 ± 0.35	44.99	42.91	0.37
NGC 3256	9.66	6.56± 0.10	0.57 ± 0.29	45.24	44.73	24.6
NGC 3310	9.62	7.24± 0.00	-0.31 ± 0.19	44.48	43.74	2.49
NGC 3351	9.13	7.32± 0.19	-0.41 ± 0.32	44.71	43.02	0.47
NGC 3507	9.12	6.69± 0.10	0.21 ± 0.27	44.55	-	-
NGC 3556	9.90	6.80± 0.09	0.14 ± 0.19	44.94	43.65	2.04
NGC 3631	9.51	6.78± 0.09	0.08 ± 0.21	44.68	43.27	0.84
NGC 3683	9.33	7.21± 0.13	-0.34 ± 0.23	44.68	43.66	2.06
NGC 3898	9.39	6.72± 0.10	0.04 ± 0.33	44.87	42.09	0.05
NGC 4136	9.43	6.91± 0.10	-0.04 ± 0.21	44.13	42.43	0.12
NGC 4151	9.39	6.52± 0.09	0.24 ± 0.33	44.87	42.90	0.36
NGC 4303	9.77	6.83± 0.09	0.09 ± 0.21	45.12	43.77	2.70
NGC 4314	7.36	4.80± 0.22	1.96 ± 0.39	44.87	42.75	0.25
NGC 4485	9.10	7.30± 0.10	-0.36 ± 0.19	43.38	-	-
NGC 4490	9.98	7.31± 0.09	-0.36 ± 0.19	44.67	43.61	1.85
NGC 4594	8.33	5.71± 0.09	1.05 ± 0.33	45.29	42.48	0.13
NGC 5728	9.19	6.45± 0.13	0.31 ± 0.34	45.02	43.55	1.63
NGC 5746	9.42	6.25± 0.09	0.65 ± 0.27	45.23	42.74	0.25
NGC 5775	9.60	6.94± 0.09	-0.03 ± 0.27	44.87	43.72	2.37
NGC 5879	9.10	6.81± 0.10	0.11 ± 0.21	44.18	42.60	0.18
NGC 6503	9.25	7.03± 0.10	-0.08 ± 0.19	44.15	42.48	0.13
NGC 7331	10.0	6.81± 0.09	0.09 ± 0.27	45.28	43.73	2.45
NGC 7714	9.16	6.72± 0.07	0.18 ± 0.27	44.52	43.71	2.33
NGC 7727	8.55	5.68± 0.26	1.08 ± 0.41	44.99	-	-

Table 5.5: Results of the Fits and Correlation study

Plot	m	c	chisq	q	spearman coeff	prob
L_X vs L_{FIR}	0.762 ± 0.014	6.625 ± 0.619	1214.1	0.0	0.78	≤0.000
L_X vs L_{FIR} normals	-0.037 0.0706	40.98 3.030	236.32	0.0	0.375	0.1854
L_X vs L_{FIR} starburst	0.9088 0.0213	0.1552 0.9408	793.9	0.0	0.757	0.00043
L_X vs L_K	0.7460 0.017584	6.5293 0.79182	2811.92	0.00	0.466	0.054
L_X vs L_K normals	0.6343 0.05866	10.9664 2.6289	119.320	0.0	0.723	0.0034
L_X vs L_K starburst	0.59229 0.020455	13.5241 0.921773	1767.71	0.0	0.186	0.474
L_X/L_K vs L_{FIR}/L_K	0.564 ± 0.088	-4.437 ± 0.140	2.602	1.0	0.767	≤0.000
$L_X/{D_{25}}^2$ vs $SFR/{D_{25}}^2$	0.0092 ± 0.0013	-0.337 ± 0.050	0.0003	1.0	0.77	≤0.000
$L_X/{D_{25}}^2$ vs $SFR/{D_{25}}^2$ for (SFR>1 $M\odot\ yr^{-1}$)	0.0090 ± 0.0021	-0.328 ± 0.0787	0.0002	1.0	0.82	≤0.000
H I sd vs $L_{FIR}/{D_{25}}^2$	0.529 ± 0.019	-14.68 ± 0.819	512.3	0.0	0.39	0.029
H I mass vs log(SFR)	0.37 0.14	9.37 0.08	27.32	0.55	0.45	0.010
H I def vs L_X/L_K	-0.254 ± 0.093	-1.234 ± 0.485	70.75	≤0.000	-0.26	0.127
H I def vs L_X/L_K for normals	-0.3510 ± 0.123	-1.8505 ± 0.6323	21.3	0.092	-0.45	7.5%
H I def vs L_X/L_K for AGN hosts	0.089 ± 0.152	0.746 ±0.816	33.9	0.0055	0.28	25.7%

5.6 Appendix to Chapter 5: X-ray images and spectra of the sample galaxies

This section contains a short note about each galaxy, mainly available literature on its interaction or merger history (an information which was useful in explaining some of our results), followed by a diffuse X-ray image (0.3 to 2 keV) overlayed on the optical image (from DSS) of the galaxy and a table containing its diffuse emission model fit parameters. The images are of low resolution (~20"), smoothed using a gaussian, from the original high resolution images, to get a better estimate of the extent of the diffuse emission.

NGC 278

NGC 278 is a small non-barred galaxy, which has a bright star forming inner region of about 2 kpc in diameter, which looks like nuclear rings seen mainly in barred galaxies. It is part of the local supercluster of galaxies centred around the Virgo cluster [149]. Arp & Sulentic (1985) in their analysis of groups of galaxies, listed NGC 278 as having a companion dwarf galaxy UGC 672 [4]. The H I morphology and kinematics of NGC 278, especially in the outer parts of the disk, show evidence for a recent interaction.

Table 5.6: Fit parameters: NGC 278

model parameter	unit	value
powerlaw Index		2.18 ± 0.259
powerlaw normalisation		$2.988\times10^{-5} \pm 0.678\times10^{-5}$
mekal kT	keV	0.45 ± 0.033
mekal nH	cm^{-3}	4.28×10^{-5} (frozen)
mekal Abundance		1.0 (frozen)
mekal redshift		2.128×10^{-3} (frozen)
mekal normalisation		$2.063\times10^{-5} \pm 0.485\times10^{-5}$

NGC 891

A nearby edge-on spiral galaxy, NGC891, has more abundant star formation than a normal spiral, but does not have as extreme properties as starburst galaxies like NGC 253 and 4945,

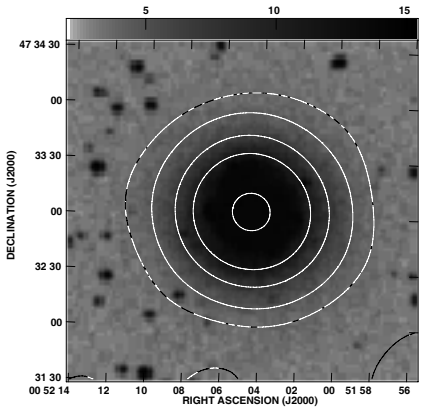

Figure 5.22: NGC 278

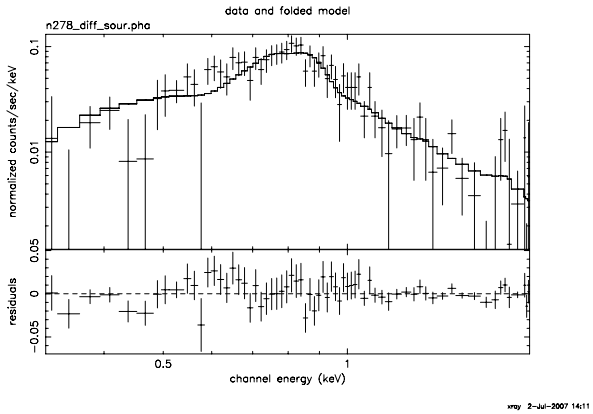

Figure 5.23: X-ray spectra (0.3 - 2.0 keV) of NGC 278

and that it is most likely a starburst galaxy in a quiescent state [141]. It is known to have extraplanar HI distribution and a recent studies show that the galaxy possess a huge gaseous halo, much more extended than seen previously and containing almost 30 % of the H I [103].

Table 5.7: Fit parameters: NGC 891

model parameter	unit	value
powerlaw Index		1.67 ± 0.23
powerlaw normalisation		$8.18\times10^{-5} \pm 1.5\times10^{-5}$
mekal kT	keV	0.219 ± 0.026
mekal nH	cm^{-3}	2.87×10^{-5} (frozen)
mekal Abundance		1.0 (frozen)
mekal redshift		1.76×10^{-3} (frozen)
mekal normalisation		$2.30\times10^{-5} \pm1.8 \times10^{-5}$

NGC 1068

NGC 1068, is one of the extensively studied Seyfert galaxies for many years at optical, UV, IR, radio, and X-ray wavelengths. H I observation with the VLA indicates substantial warping of the disk [16]. Due to the presence of the strong central source in this galaxy, the diffuse emission from NGC 1068 has been modelled in a different way than the rest of the sample. The central source was modelled first with an absorbed power law that resulted in an index value of 2.68 ± 0.793. The diffuse emission region was then modelled with a pow +

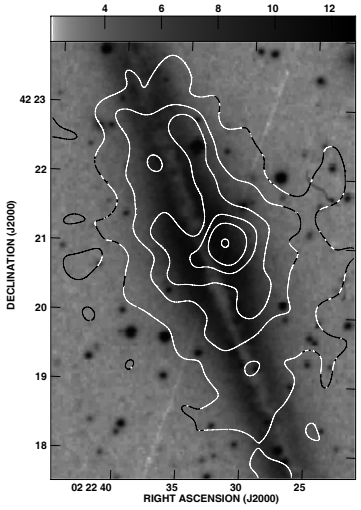

Figure 5.24: NGC 891

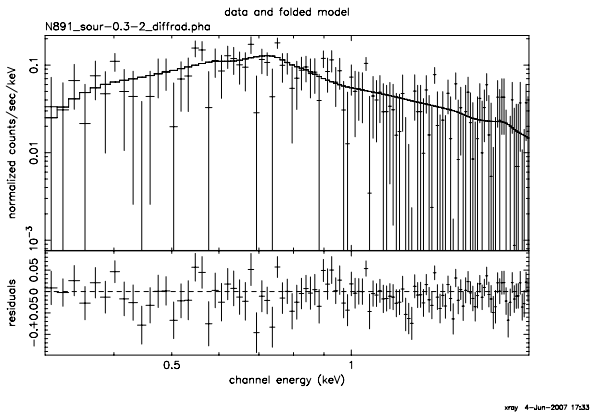

Figure 5.25: X-ray spectra (0.3 - 2.0 keV) of NGC 891

mekal model with the central source included. The power law index in the model was frozen at 2.68. While retrieving the flux value, the power law normalisation parameter was set to zero, so that only the mekal model contribution is visible.

Table 5.8: Fit parameters: NGC 1068

model parameter	unit	value
powerlaw Index		2.68 ± 0.793 (frozen)
powerlaw normalisation		$1.311 \times 10^{-3} \pm 1.4 \times 10^{-3}$
mekal kT	keV	0.618 ± 0.0032
mekal nH	cm^{-3}	9.600×10^{-6} (frozen)
mekal Abundance		1.0 (frozen)
mekal redshift		3.79×10^{-3} (frozen)
mekal normalisation		$7.74 \times 10^{-4} \pm 0.23 \times 10^{-4}$

NGC 1808

NGC 1808 is a nearby starburst galaxy also hosting an AGN ([75]). Earlier studies of this galaxy suggest that the starburst activity in this galaxy may have been introduced by a tidal interaction with a nearby galaxy NGC 1792([152][82]).

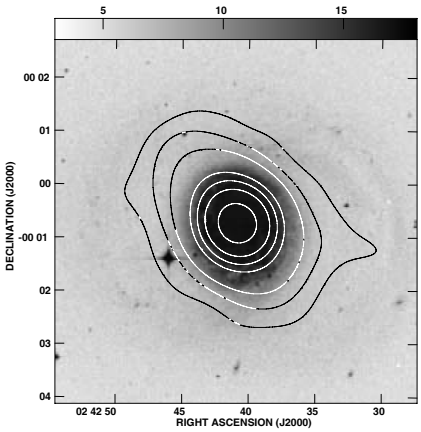

Figure 5.26: NGC 1068

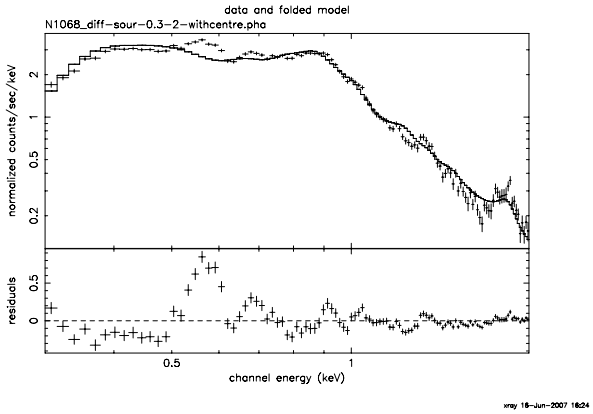

Figure 5.27: X-ray spectra (0.3 - 2.0 keV) of NGC 1068

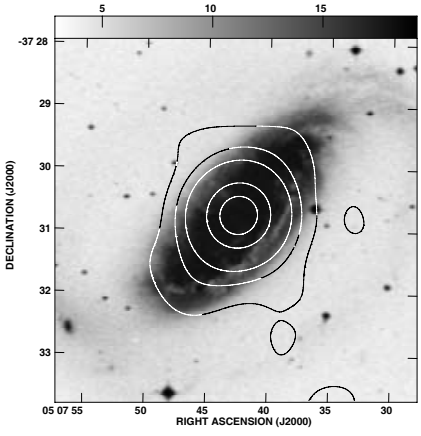

Figure 5.28: NGC 1808

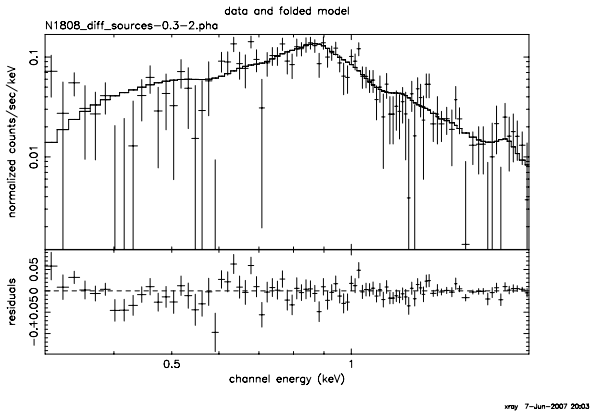

Figure 5.29: X-ray spectra (0.3 - 2.0 keV) of NGC 1808

Table 5.9: Fit parameters: NGC 1808

model parameter	unit	value
powerlaw Index		2.18 ±0.15
powerlaw normalisation		$5.691 \times 10^{-5} \pm 1.11 \times 10^{-5}$
mekal kT	keV	0.606 ±0.022
mekal nH	cm^{-3}	7.57×10^{-6} (frozen)
mekal Abundance		1.0 (frozen)
mekal redshift		3.319×10^{-3} (frozen)
mekal normalisation		$5.14 \times 10^{-5} \pm 1.19 \times 10^{-5}$

NGC 2146

NGC 2146 is a starbusrt spiral galaxy immersed in a extended H I structure that has morphological and kinematical resemblance to a strong tidal interaction. VLA H I observations reveal elongated streams of neutral hydrogen not in the principle plane of rotation of the galaxy, but instead are suggestive of a tidal interaction between NGC 2146 and a less massive but gas-rich LSB companion that was destroyed by the encounter and remains undetected at optical wavelengths. The H I morphology of this galaxy is disturbed, but the interaction was such that the spiral disk was retained. Analysis of the trajectory of the outlying gas suggests that the closest encounter took place about 0.8×10^9 years ago and that infall of debris will continue for a similar time span ([140]).

Table 5.10: Fit parameters: NGC 2146

model parameter	unit	value
powerlaw Index		1.40 ±0.373
powerlaw normalisation		$1.44 \times 10^{-4} \pm 0.590 \times 10^{-4}$
mekal kT	keV	0.646 ±0.0431
mekal nH	cm^{-3}	2.04×10^{-5} (frozen)
mekal Abundance		1.0 (frozen)
mekal redshift		2.979×10^{-3} (frozen)
mekal normalisation		$1.255 \times 10^{-4} \pm 0.605 \times 10^{-4}$

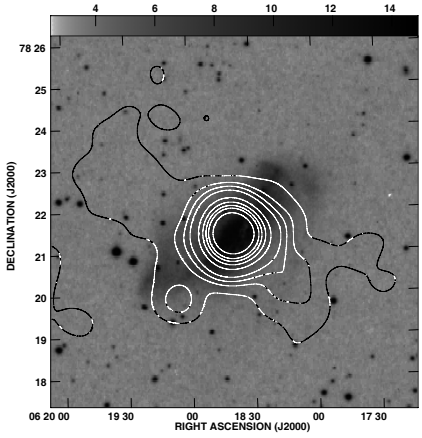

Figure 5.30: NGC 2146

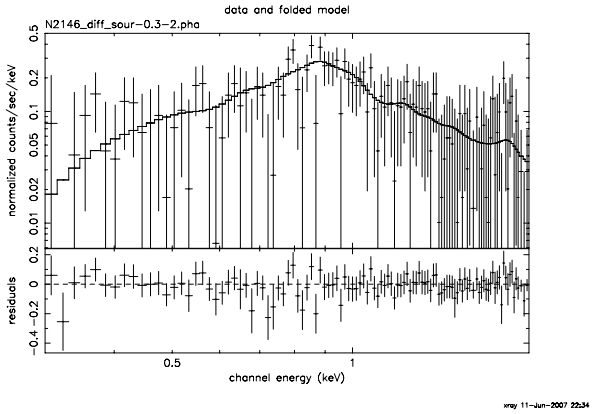

Figure 5.31: X-ray spectra (0.3 - 2.0 keV) of NGC 2146

NGC 2276

NGC 2276 a starburst spiral of the NGC 2300 group of galaxies, owes most of its star formation activity to a strong galaxy interaction with hot intra-group gas. Observations show the intra-group gas being pressurised at the leading western edge of NGC 2276 due to the galaxy moving supersonically through the IGM at a velocity $\sim$ 850 km s^{-1} . Evidence supporting this interpretation is the high star formation rate (SFR) of NGC 2276 , with much of this starburst activity occurring along the western edge, as expected if an interaction with the IGM has triggered some of the star formation via ram-pressure compression of molecular gas [113].

Table 5.11: Fit parameters: NGC 2276

model parameter	unit	value
powerlaw Index		2.27±0.27
powerlaw normalisation		2.59×10^{-5} $\pm 0.77 \times 10^{-5}$
mekal kT	keV	0.66 ± 0.03
mekal nH	cm^{-3}	0.84×10^{-5} (frozen)
mekal Abundance		1.0 (frozen)
mekal redshift		8.0×10^{-3} (frozen)
mekal normalisation		2.59×10^{-5} $\pm 0.91 \times 10^{-5}$

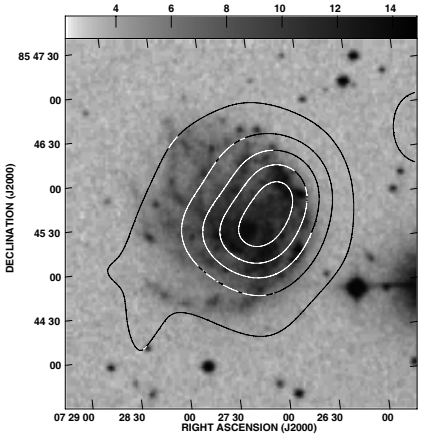

Figure 5.32: NGC 2276

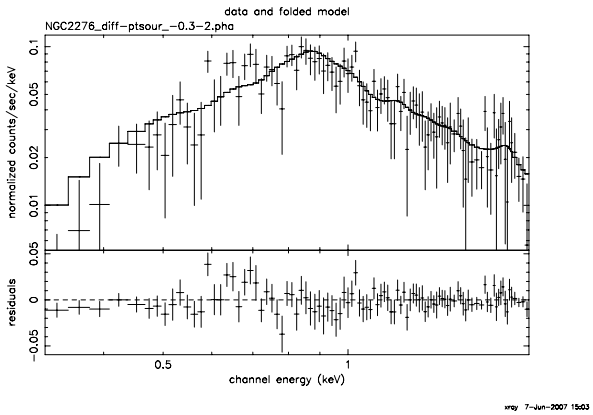

Figure 5.33: X-ray spectra (0.3 - 2.0 keV) of NGC 2276

NGC 2782

The stellar and gaseous structure of NGC2782 suggest that either it is a merger remnant or it was gravitationally disturbed by the passage of another galaxy. Tidal tails have been discovered in this galaxy and almost 70% of the H I of this galaxy lies outside of the main body [129]. Studies show this galaxy to be a minor merger having a mass ratio of 0.25 that occurred 200 Myr ago, and it has a population of young star clusters which is formed along both tidal tails ([81]).The galaxy hosts a low luminosity AGN ([148]).

Table 5.12: Fit parameters: NGC 2782

model parameter	unit	value
powerlaw Index		1.85 ±0.455
powerlaw normalisation		$1.363 \times 10^{-5} \pm 0.58 \times 10^{-5}$
mekal kT	keV	0.47±0.038
mekal nH	cm^{-3}	1.926×10^{-6} (frozen)
mekal Abundance		1.0 (frozen)
mekal redshift		8.483×10^{-3} (frozen)
mekal normalisation		$1.553 \times 10^{-5} \pm 0.476 \times 10^{-5}$

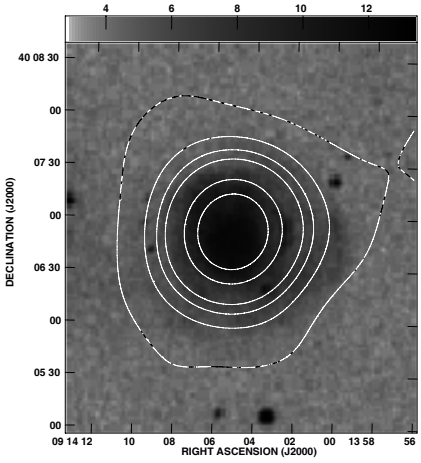

Figure 5.34: NGC 2782

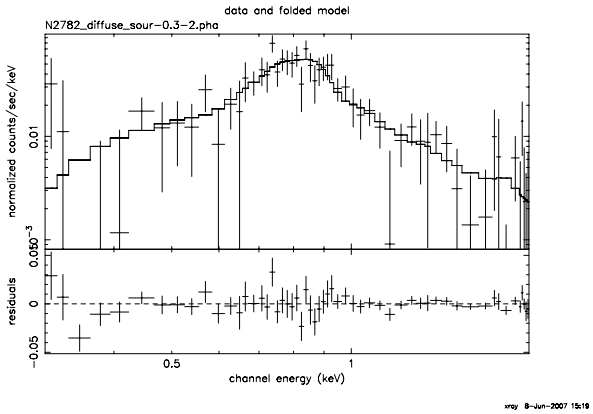

Figure 5.35: X-ray spectra (0.3 - 2.0 keV) of NGC 2782

NGC 2841

NGC 2841 is an isolated barred galaxy harbouring a low luminosity AGN ([99]). FIR observations show dust to be distributed in a ring around the galaxy ([77]). H I observations of this galaxy show the presence of a hole in the centre whose size corresponds to the bulge. The outer H I structure has an orientation that differs from the main body of the galaxy ([14]).

Table 5.13: Fit parameters: NGC 2841

model parameter	unit	value
powerlaw Index		1.98 ±0.37
powerlaw normalisation		$7.79 \times 10^{-5} \pm 2.20 \times 10^{-5}$
mekal kT	keV	0.219 ±0.045
mekal nH	cm^{-3}	0.32×10^{-5} (frozen)
mekal Abundance		1.0 (frozen)
mekal redshift		2.1×10^{-3} (frozen)
mekal normalisation		$2.50 \times 10^{-5} \pm 3.07 \times 10^{-5}$

NGC 3079

NGC 3079 is a spiral galaxy hosting a double-lobed AGN ([71]). The galaxy is known to be the source of strong superwind that is stripping H I away from its dwarf S0 companion

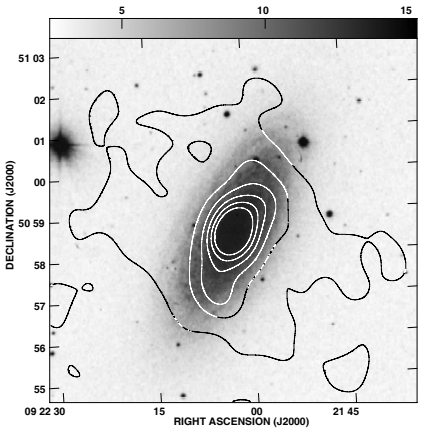

Figure 5.36: NGC 2841

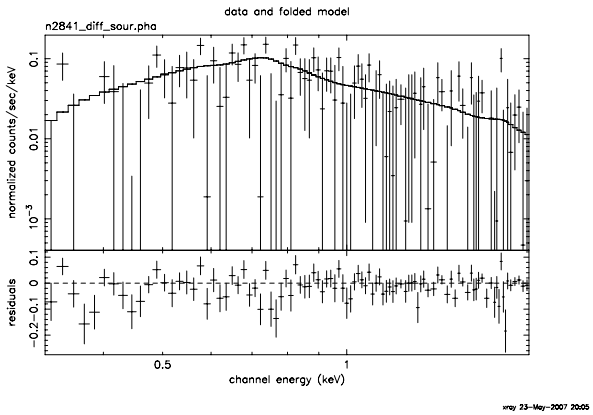

Figure 5.37: X-ray spectra (0.3 - 2.0 keV) of NGC 2841

NGC 3073 ([73]). H I observations of this galaxy reveal that the galaxy has been perturbed at some point in it's history, strongly enough to disturb its H I and optical disk, but not so severe to disrupt the galaxies' smooth density and velocity distributions. The position of the assymetry of the perturbation suggests a close encounter from a more massive galaxy than the two existing companions NGC 3073 and MCG 09-17-09 ([72]). This idea is further supported by the studies that show nuclear outflows can result from tidal perturbations, not only in AGNs but in starbursts as well ([63]).

Table 5.14: Fit parameters: NGC 3079

model parameter	unit	value
powerlaw Index		2.2 ± 0.171
powerlaw normalisation		$8.82 \times 10^{-5} \pm 2.20 \times 10^{-5}$
mekal kT	keV	0.547 ± 0.031
mekal nH	cm^{-3}	1.56×10^{-6} (frozen)
mekal Abundance		1.0 (frozen)
mekal redshift		3.7×10^{-3} (frozen)
mekal normalisation		$6.96 \times 10^{-5} \pm 2.0 \times 10^{-5}$

NGC 3184

NGC 3184 is a face on nearby spiral galaxy. It does not have any evidence for an AGN and the nuclear region has an HII region spectrum ([85]).

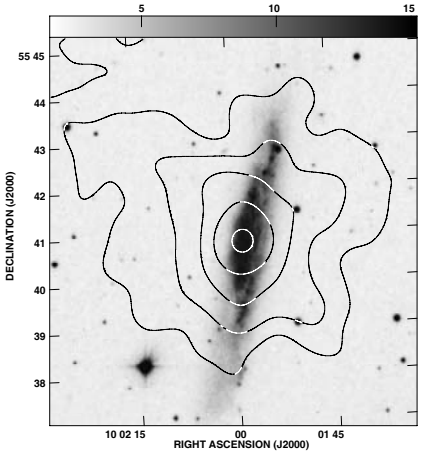

Figure 5.38: NGC 3079

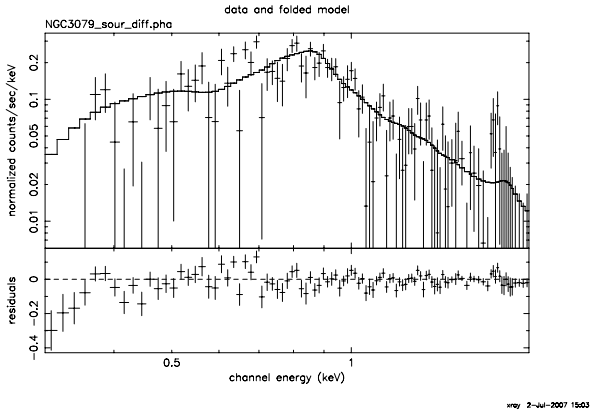

Figure 5.39: X-ray spectra (0.3 - 2.0 keV) of NGC 3079

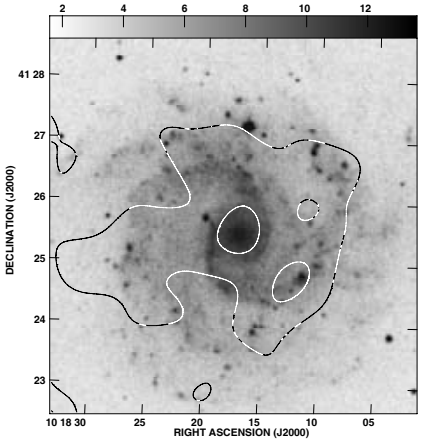

Figure 5.40: NGC 3184

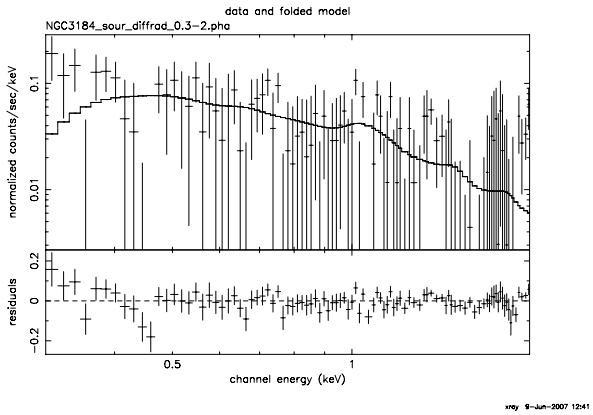

Figure 5.41: X-ray spectra (0.3 - 2.0 keV) of NGC 3184

Table 5.15: Fit parameters: NGC 3184

model parameter	unit	value
powerlaw Index		2.32 ±0.36
powerlaw normalisation		$4.28 \times 10^{-5} \pm 3.09 \times 10^{-5}$
mekal kT	keV	1.15 ±0.49
mekal nH	cm^{-3}	3.270×10^{-6} (frozen)
mekal Abundance		1.0 (frozen)
mekal redshift		1.975×10^{-3} (frozen)
mekal normalisation		$1.827 \times 10^{-5} \pm 6.02 \times 10^{-5}$

NGC 3190

NGC 3190 is the brightest spiral galaxy of Hickson Compact Group 44. H I observation of the group shows that the three brightest spirals of this group have experienced recent tidal interactions. In channel maps of VLA observation of this group, very weak H I emission can be seen between NGC 3190 and NGC3185. The bridge of faint H I emission, the misalignment of the H I and the optical disk and the warping in the outer parts of NGC 3187, all are signs of this recent interaction ([159]).

Table 5.16: Fit parameters: NGC 3190

model parameter	unit	value
powerlaw Index		2.36 ±0.355
powerlaw normalisation		$1.82 \times 10^{-5} \pm 0.95 \times 10^{-5}$
mekal kT	keV	0.58 ± 0.21
mekal nH	cm^{-3}	0.401×10^{-5} (frozen)
mekal Abundance		1.0 (frozen)
mekal redshift		4.2×10^{-3} (frozen)
mekal normalisation		$4.35 \times 10^{-6} \pm 8.8 \times 10^{-6}$

NGC 3256

NGC3256 is a well known merger induced starburst galaxy with double nuclei and tidal tails [110]. The total IR luminosity of this galaxy is 6×10^{11} $L_{\odot}$, which is only a factor of 2 lower than the ultraluminous IR galaxies, making it the most IR luminous galaxy known at z <

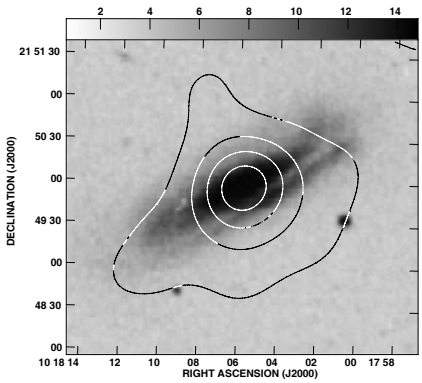

Figure 5.42: NGC 3190

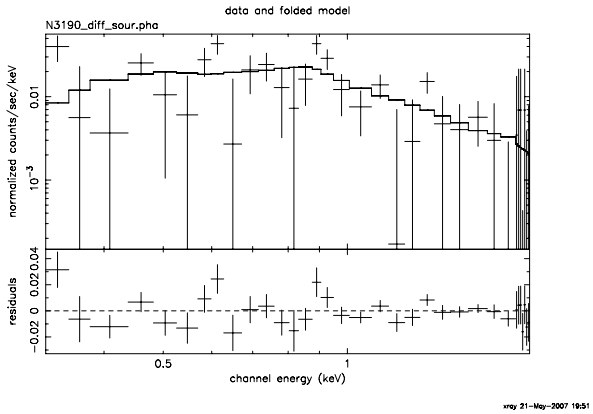

Figure 5.43: X-ray spectra (0.3 - 2.0 keV) of NGC 3190

0.01. Studies have also shown the presence of a low luminosity AGN in this galaxy ([84]).

Table 5.17: Fit parameters: NGC 3256

model parameter	unit	value
powerlaw Index		1.21 ±0.24
powerlaw normalisation		$1.29 \times 10^{-4} \pm 0.32 \times 10^{-4}$
mekal kT	keV	0.67 ± 0.01
mekal nH	cm^{-3}	9.900×10^{-6} (frozen)
mekal Abundance		1.0 (frozen)
mekal redshift		9.354×10^{-3} (frozen)
mekal normalisation		$1.421 \times 10^{-4} \pm 0.246 \times 10^{-4}$

NGC 3310

NGC 3310 is a nearby spiral undergoing an intense starburst. This is an isolated galaxy which displays signs of merger. Studies suggest it is likely that the disk of NGC3310 is growing through the accretion of multiple, small companions on to a pre-existing disc ([158]).

NGC 3351

NGC 3351 is a barred spiral undergoing starburst.

NGC 3507

The spiral NGC 3507 is a barred galaxy, with two long regular symmetric arms circling

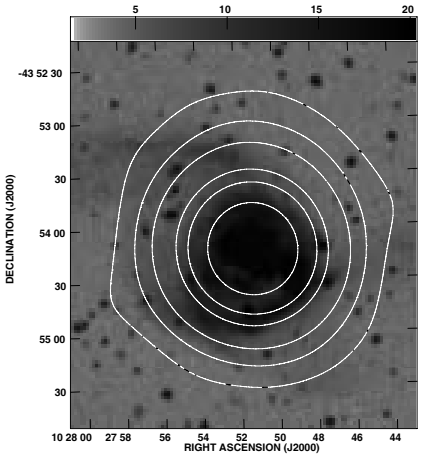

Figure 5.44: NGC 3256

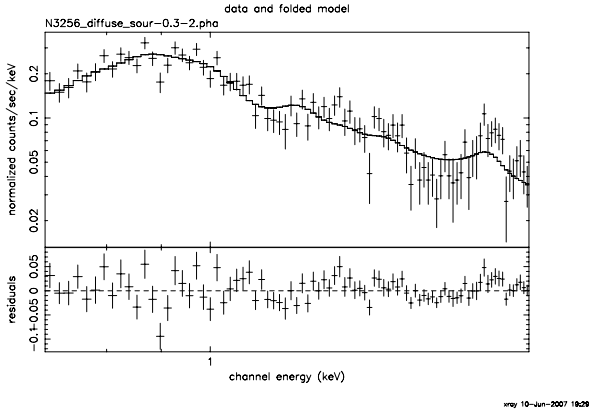

Figure 5.45: X-ray spectra (0.3 - 2.0 keV) of NGC 3256

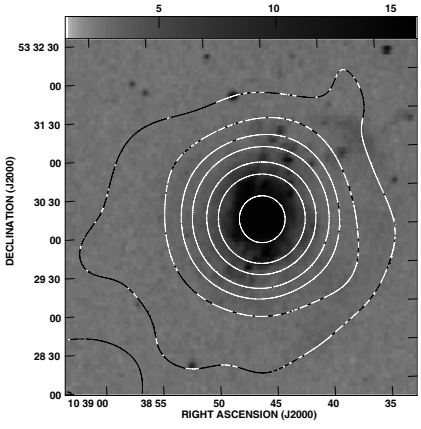

Figure 5.46: NGC 3310

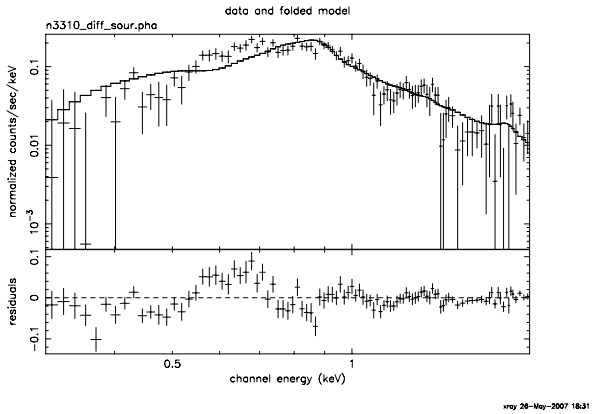

Figure 5.47: X-ray spectra (0.3 - 2.0 keV) of NGC 3310

Table 5.18: Fit parameters: NGC 3310

model parameter	unit	value
powerlaw Index		2.27 ± 0.09
powerlaw normalisation		$8.21 \times 10^{-5} \pm 0.98 \times 10^{-5}$
mekal kT	keV	0.527 ± 0.018
mekal nH	cm^{-3}	2.19×10^{-6} (frozen)
mekal Abundance		1.0 (frozen)
mekal redshift		3.312×10^{-3} (frozen)
mekal normalisation		$6.24 \times 10^{-5} \pm 0.98 \times 10^{-5}$

Table 5.19: Fit parameters: NGC 3351

model parameter	unit	value
powerlaw Index		2.63 ± 0.50
powerlaw normalisation		$1.44 \times 10^{-5} \pm 0.59 \times 10^{-5}$
mekal kT	keV	0.32 ± 0.33
mekal nH	cm^{-3}	0.10×10^{-4} (frozen)
mekal Abundance		1.0 (frozen)
mekal redshift		2.5×10^{-3} (frozen)
mekal normalisation		$1.088 \times 10^{-5} \pm 0.325 \times 10^{-5}$

around the nucleus and the bar. It is the host of a low luminosity AGN. This galaxy is in pair with NGC 3501 but no study exists about their level of interaction.

Table 5.20: Fit parameters: NGC 3507

model parameter	unit	value
powerlaw Index		2.15 ± 0.62
powerlaw normalisation		$0.09 \times 10^{-5} \pm 0.044 \times 10^{-5}$
mekal kT	keV	0.176 ±0.036
mekal nH	cm^{-3}	3.30×10^{-6} (frozen)
mekal Abundance		1.0 (frozen)
mekal redshift		3.26×10^{-3} (frozen)
mekal normalisation		$3.45 \times 10^{-6} \pm 1.04 \times 10^{-6}$

NGC 3556

NGC 3556 is a late type close to edge on galaxy. The galaxy has no obvious interacting companion. Observation show existence of H I supershells in the galaxy, which the authors

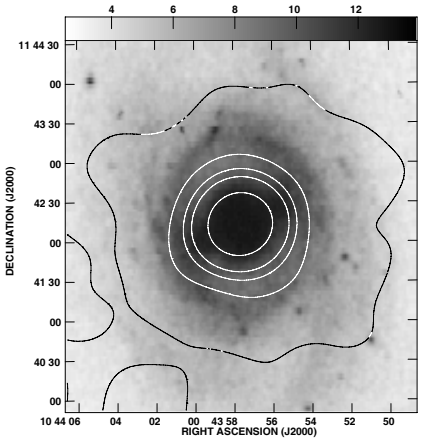

Figure 5.48: NGC 3351

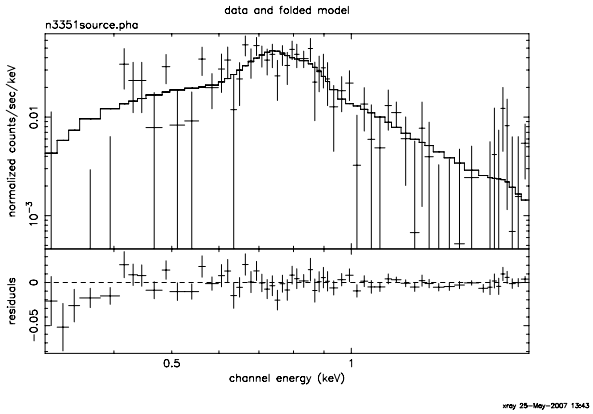

Figure 5.49: X-ray spectra (0.3 - 2.0 keV) of NGC 3351

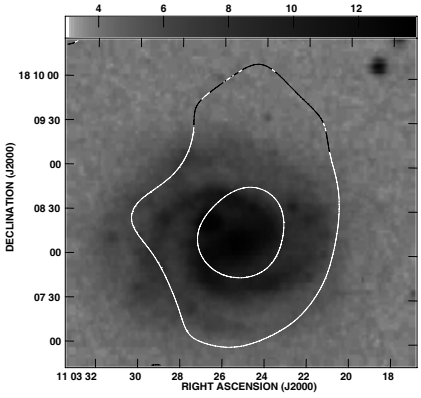

Figure 5.50: NGC 3507

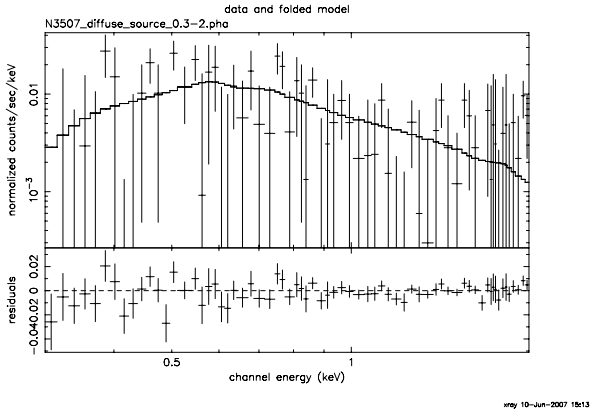

Figure 5.51: X-ray spectra (0.3 - 2.0 keV) of NGC 3507

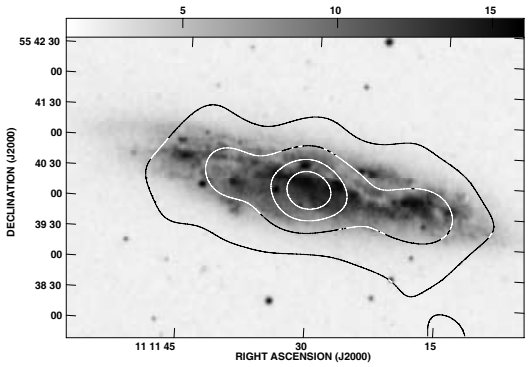

Figure 5.52: NGC 3556

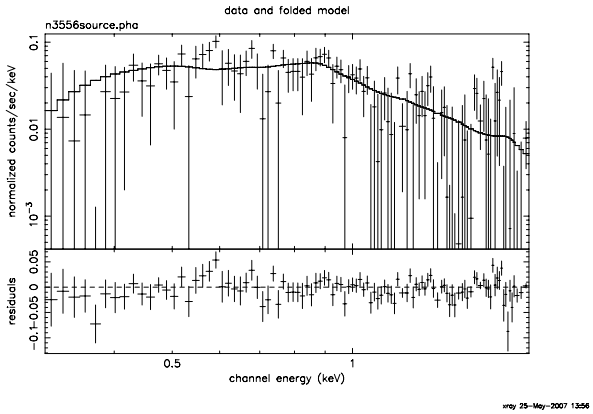

Figure 5.53: X-ray spectra (0.3 - 2.0 keV) of NGC 3556

interpret is due to radio jets in NGC 3556 which are currently too weak for detection ([55]).

Table 5.21: Fit parameters: NGC 3556

model parameter	unit	value
powerlaw Index		2.42 ± 0.18
powerlaw normalisation		4.41×10^{-5} ± 1.24×10^{-5}
mekal kT	keV	0.59 ± 0.06
mekal nH	cm^{-3}	1.83×10^{-6} (frozen)
mekal Abundance		1.0 (frozen)
mekal redshift		2.33×10^{-3} (frozen)
mekal normalisation		1.21×10^{-5} ± 1.09×10^{-5}

NGC 3631

NGC 3631 is a late type face on spiral galaxy. It is non-barred, has no companions and shows no signs of important dynamical perturbations ([80]).

NGC 3683

NGC 3683 is a barred late type spiral in NGC 3642 group. Not enough detailed study exists about this galaxy in literature.

NGC 3898

NGC 3898 is a Sab type spiral galaxy. Low star formation in this galaxy can be attributed to its relatively early type morphology, as star formation history of Sa type galaxies have been

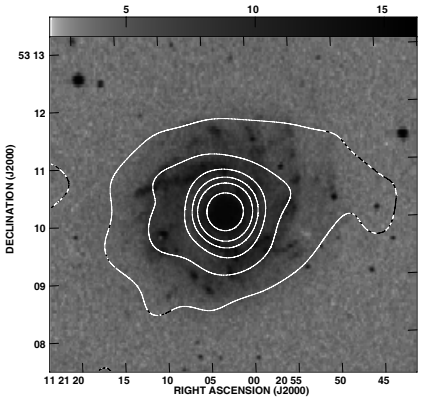

Figure 5.54: NGC 3631

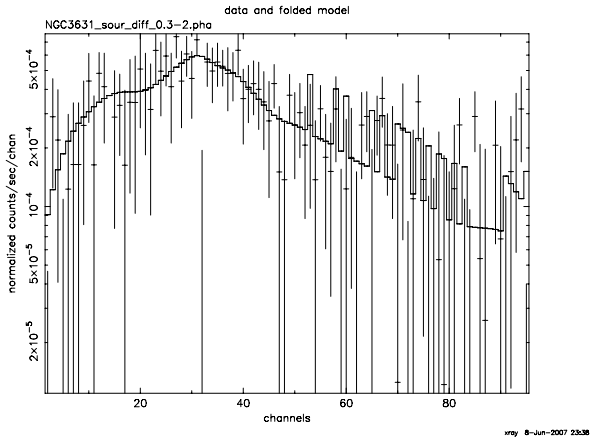

Figure 5.55: X-ray spectra (0.3 - 2.0 keV) of NGC 3631

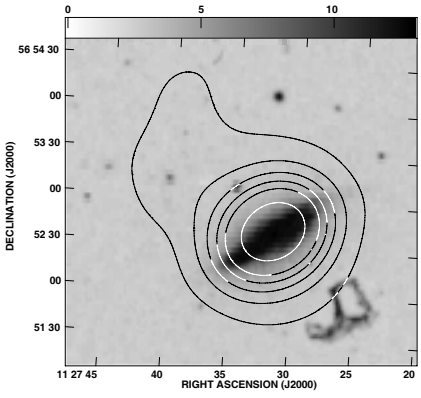

Figure 5.56: NGC 3683

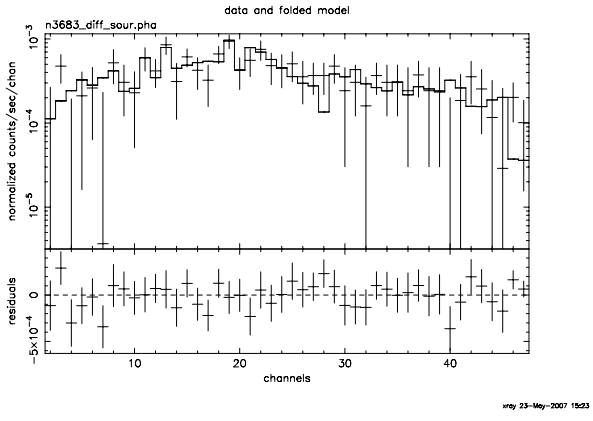

Figure 5.57: X-ray spectra (0.3 - 2.0 keV) of NGC 3683

Table 5.22: Fit parameters: NGC 3631

model parameter	unit	value
powerlaw Index		2.29 ±0.24
powerlaw normalisation		$2.829\times10^{-5} \pm 0.55 \times10^{-5}$
mekal kT	keV	0.315 ± 0.0481
mekal nH	cm^{-3}	0.0214×10^{-5} (frozen)
mekal Abundance		1.0 (frozen)
mekal redshift		3.856×10^{-3} (frozen)
mekal normalisation		$0.6105 \times10^{-5} \pm0.031 \times10^{-5}$

Table 5.23: Fit parameters: NGC 3683

model parameter	unit	value
powerlaw Index		1.22 ±0.64
powerlaw normalisation		$1.00 \times10^{-5} \pm 0.54\times10^{-5}$
mekal kT	keV	0.270 ± .028
mekal nH	cm^{-3}	1.36×10^{-6} (frozen)
mekal Abundance		1.0 (frozen)
mekal redshift		5.7×10^{-3} (frozen)
mekal normalisation		$1.06 \times10^{-5} \pm 0.43 \times10^{-5}$

found to be quite different than late type spirals([21]). H I observations show it to be gas rich but with a deep central depression, which is about 4 times the effective bulge diameter. At a projected distance of 26', there is a small irregular galaxy UGC 6816. It is 129 kpc from MGC3898 and separated in velocity by 284 km s^{-1} and there is no confirmed knowledge about them being an interacting pair [153].

Table 5.24: Fit parameters: NGC 3898

model parameter	unit	value
powerlaw Index		0.70 ± 0.80
powerlaw normalisation		$0.95\times10^{-5} \pm 0.64\times10^{-5}$
mekal kT	keV	0.16 ± 0.014
mekal nH	cm^{-3}	2.0×10^{-6} (frozen)
mekal Abundance		1.0 (frozen)
mekal redshift		3.92×10^{-3} (frozen)
mekal normalisation		$1.51\times10^{-5} \pm 0.93\times10^{-5}$

i

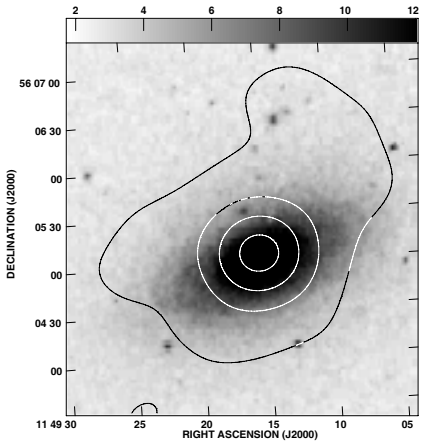

Figure 5.58: NGC 3898

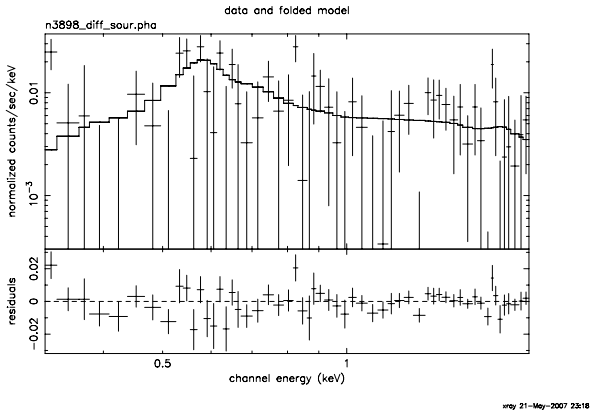

Figure 5.59: X-ray spectra (0.3 - 2.0 keV) of NGC 3898

NGC 4136

NGC 4136 is a gas rich late type spiral in NGC 4062 group. The H I distribution of this galaxy is normal with no visible distortions ([2]). The galaxy is without any obvious companion and the nearest galaxy with a comparable radial velocity is 77' away.

Table 5.25: Fit parameters: NGC 4136

model parameter	unit	value
powerlaw Index		1.67±1.02
powerlaw normalisation		$9.96 \times 10^{-6} \pm 5.72 \times 10^{-5}$
mekal kT	keV	0.35 ± 0.22
mekal nH	cm^{-3}	3.50×10^{-6} (frozen)
mekal Abundance		1.0 (frozen)
mekal redshift		2.03×10^{-3} (frozen)
mekal normalisation		$1.59 \times 10^{-5} \pm 2.8 \times 10^{-5}$

NGC 4151

NGC 4151 is a nearby Sab type grand-design, Seyfert 1, barred spiral galaxy. The bar shows evidence of most of the active star formation, with two faint outer spiral arms visible only in deep optical images. The bar is unusually gas-rich and has been studied in detail by Mundell & Shone (1999)[98] who find the presence of shocks and inflows along the bar.

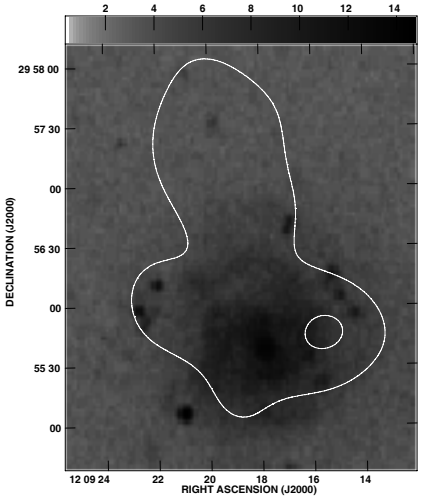

Figure 5.60: NGC 4136

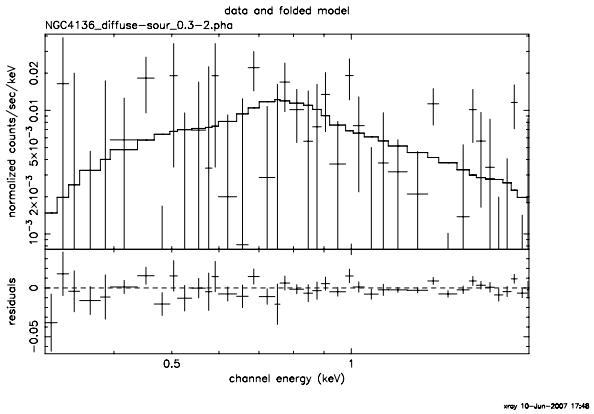

Figure 5.61: X-ray spectra (0.3 - 2.0 keV) of NGC 4136

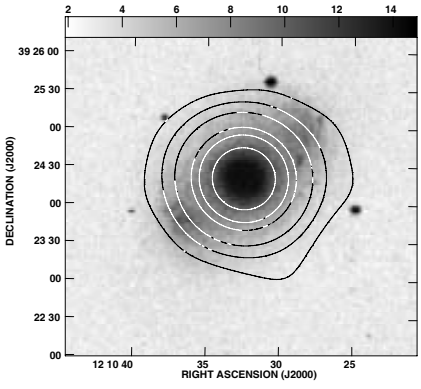

Figure 5.62: NGC 4151

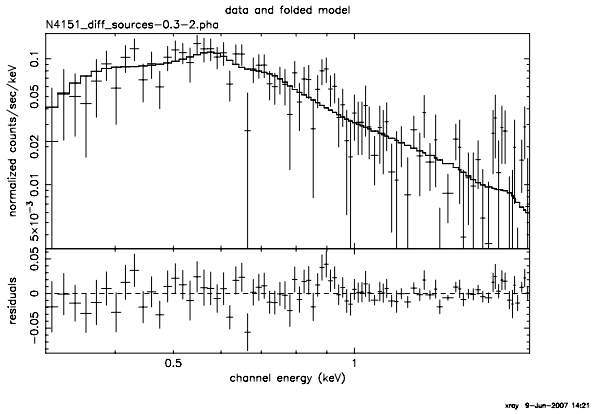

Figure 5.63: X-ray spectra (0.3 - 2.0 keV) of NGC 4151

Table 5.26: Fit parameters: NGC 4151

model parameter	unit	value
powerlaw Index		2.28 ±0.14
powerlaw normalisation		$4.455 \times 10^{-5} \pm 0.650 \times 10^{-5}$
mekal kT	keV	0.1716 ±0.766
mekal nH	cm^{-3}	0.44×10^{-5} (frozen)
mekal Abundance		1.0 (frozen)
mekal redshift		3.319×10^{-3} (frozen)
mekal normalisation		$2.294 \times 10^{-5} \pm 1.36 \times 10^{-5}$

NGC 4303

NGC 4303 (M61) is a nearby, widely studied barred galaxy harboring a low-luminosity AGN.

Table 5.27: Fit parameters: NGC 4303

model parameter	unit	value
powerlaw Index		2.73 ±0.13
powerlaw normalisation		$1.031 \times 10^{-4} \pm 0.193 \times 10^{-4}$
mekal kT	keV	0.323 ± 0.0312
mekal nH	cm^{-3}	0.036×10^{-5} (frozen)
mekal Abundance		1.0 (frozen)
mekal redshift		5.2240×10^{-3} (frozen)
mekal normalisation		$3.810 \times 10^{-5} \pm 0.896 \times 10^{-5}$

NGC 4314

NGC 4314 is a barred spiral with very high H I deficiency. It has almost 100 times less H I compared to a spiral of similar morphology. Observations reveal the reason for this deficiency to be firstly the effect of ram pressure stripping by the intra-cluster medium and secondly by an earlier tidal interaction with a neighbour. It is seen that most of the remaining gas is in molecular form in this galaxy and is also forming stars, which may have resulted by the gas being pushed from the outer regions to the inner region ([49]).

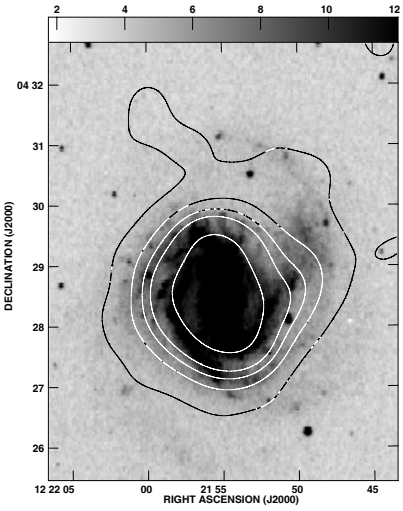

Figure 5.64: NGC 4303

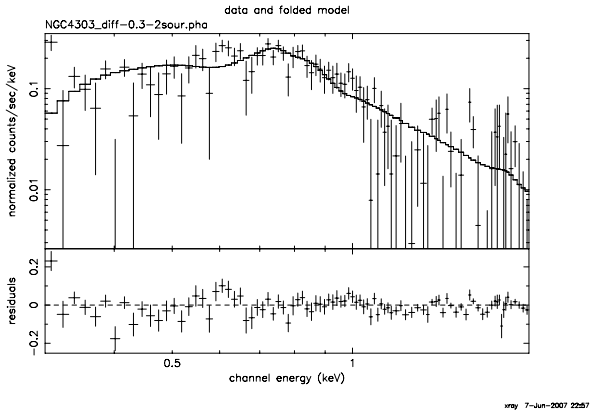

Figure 5.65: X-ray spectra (0.3 - 2.0 keV) of NGC 4303

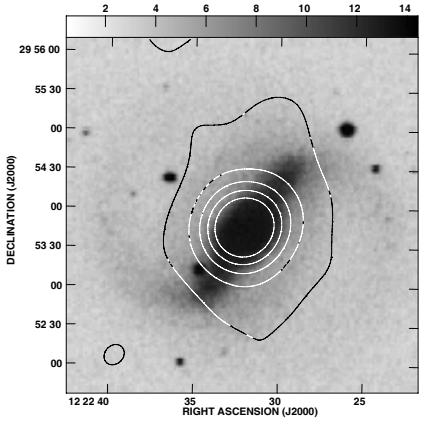

Figure 5.66: NGC 4314

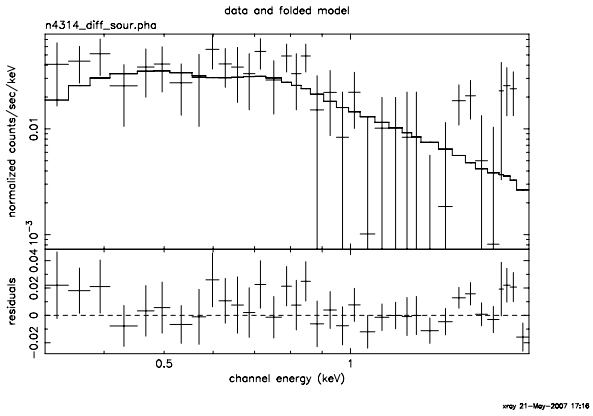

Figure 5.67: X-ray spectra (0.3 - 2.0 keV) of NGC 4314

Table 5.28: Fit parameters: NGC 4314

model parameter	unit	value
powerlaw Index		2.64 ± 0.34
powerlaw normalisation		2.27×10^{-5} ± 1.30×10^{-5}
mekal kT	keV	0.29 ±0.09
mekal nH	cm^{-3}	0.34 $\times10^{-5}$ (frozen)
mekal Abundance		1.0 (frozen)
mekal redshift		3.21 $\times10^{-3}$ (frozen)
mekal normalisation		2.1×10^{-6} ± 6.5×10^{-6}

NGC 4485/4490

NGC 4490 and NGC 4485 is an interacting pair of spirals. Observations shows ongoing star formation over the entire disc of NGC 4490. There are further evidence that the effects of the interaction have not had sufficient time to affect the star formation rate in NGC 4490 significantly, although NGC 4485 has been severely affected by the interaction ([30]).

Table 5.29: Fit parameters: NGC 4485

model parameter	unit	value
powerlaw Index		2.23 ± 0.39
powerlaw normalisation		0.71 $\times10^{-5}$ ± 0.24×10^{-5}
mekal kT	keV	0.336 ±0.093
mekal nH	cm^{-3}	0.050 $\times10^{-5}$ (frozen)
mekal Abundance		1.0 (frozen)
mekal redshift		1.64×10^{-3} (frozen)
mekal normalisation		0.148 $\times10^{-5}$ ± 0.12 $\times10^{-5}$

NGC 4594

NGC 4594, the well known Sombrero, shows no signs of interaction even on the deepest optical images, nor is there anything unusual in the H I distribution or velocity structure, and though the H I mass is unusually small, there is no evidence of large radial velocities [5]. However, observations show a faint feature at a considerable projected distance to the SW of the galaxy. This takes the form of a faint loop which appears to be associated with M104,

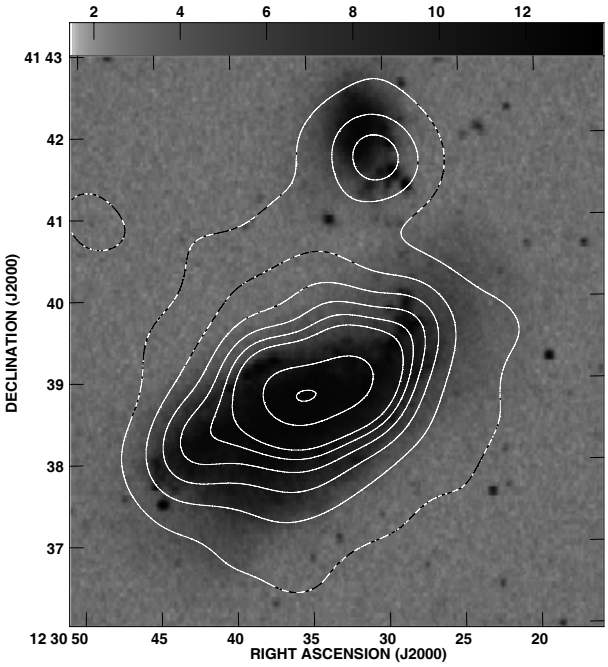

Figure 5.68: NGC 4485/4490

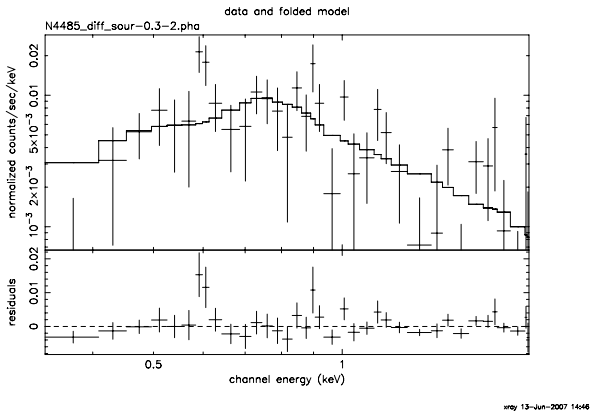

Figure 5.69: X-ray spectra (0.3 - 2.0 keV) of NGC 4485

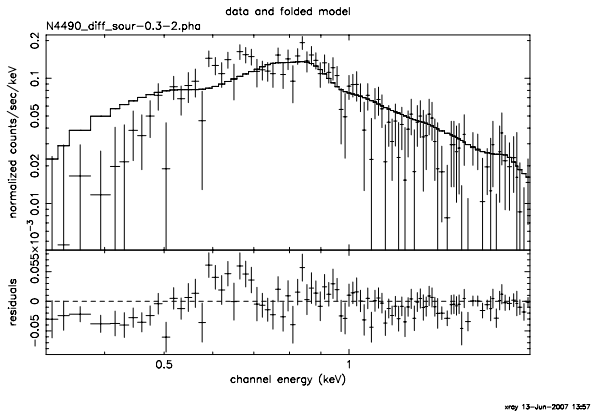

Figure 5.70: X-ray spectra (0.3 - 2.0 keV) of NGC 4490

Table 5.30: Fit parameters: NGC 4490

model parameter	unit	value
powerlaw Index		2.03 ± 0.159
powerlaw normalisation		$1.10\times10^{-4} \pm 0.11\times10^{-4}$
mekal kT	keV	0.441 ±0.024
mekal nH	cm^{-3}	5.02×10^{-6} (frozen)
mekal Abundance		1.0 (frozen)
mekal redshift		1.880×10^{-3} (frozen)
mekal normalisation		$2.26 \times10^{-5} \pm0.74 \times10^{-5}$

but, like that in M83, seemingly detached from it. There is also a strong suggestion of a more diffuse faint structure of similar extent to the NNE of the galaxy, diametrically opposed to the loop. These features strongly indicate merger activity in this galaxy [**?**].

Table 5.31: Fit parameters: NGC 4594

model parameter	unit	value
powerlaw Index		1.74 ± 0.21
powerlaw normalisation		$1.25\times10^{-4} \pm 0.3100\times10^{-4}$
mekal kT	keV	0.5421 ± 0.0522
mekal nH	cm^{-3}	1.541×10^{-5} (frozen)
mekal Abundance		1.0 (frozen)
mekal redshift		3.416×10^{-3} (frozen)
mekal normalisation		$6.529\times10^{-5} \pm 0.0324\times10^{-5}$

NGC 5728

NGC 5728 is a barred Seyfert 2 spiral. Studies done to explain the off-centre CO emission in this galaxy, suggest a recent minor merger as one of the possible ways of explaining it [107]. Simulations of minor mergers by Hernquist & Mihos (1995) [64] show evidence for molecular gas offset from the primary galaxy center. If the asymmetric CO distribution in this galaxy is the result of a minor merger, it may be responsible for triggering the large-scale bar perturbation and could account for the counter-rotating core reported by Prada & Gutirrez (1999) [109].

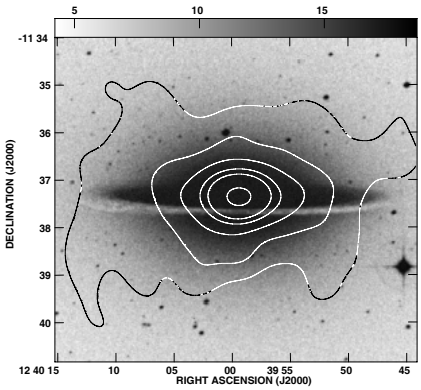

Figure 5.71: NGC 4594

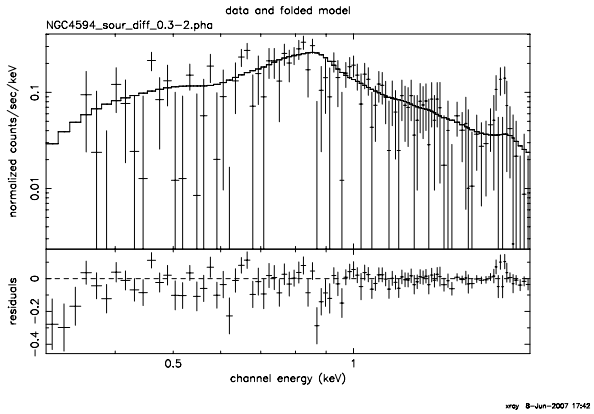

Figure 5.72: X-ray spectra (0.3 - 2.0 keV) of NGC 4594

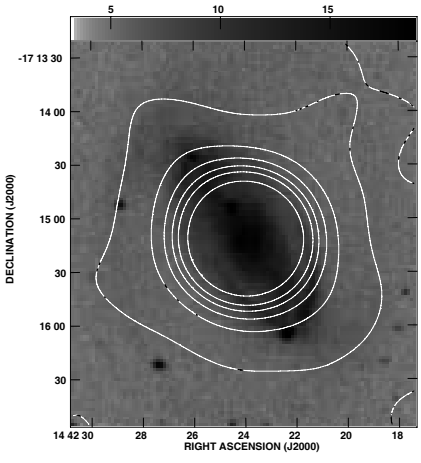

Figure 5.73: NGC 5728

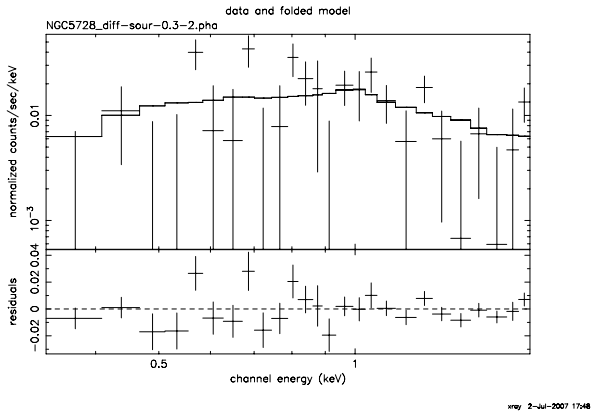

Figure 5.74: X-ray spectra (0.3 - 2.0 keV) of NGC 5728

Table 5.32: Fit parameters: NGC 5728

model parameter	unit	value
powerlaw Index		1.66 ±0.54
powerlaw normalisation		$1.70 \times 10^{-5} \pm 0.011 \times 10^{-5}$
mekal kT	keV	0.87 ± 0.24
mekal nH	cm^{-3}	1.014×10^{-5} (frozen)
mekal Abundance		1.0 (frozen)
mekal redshift		9.353×10^{-3} (frozen)
mekal normalisation		$9.98 \times 10^{-6} \pm 0.0137 \times 10^{-5}$

NGC 5746

NGC 5746 is a massive, edge on spiral galaxy showing no signs of significant star formation activity. An extended hot gas (0.2 to 3.0 keV) halo has been detected around this galaxy from Chandra X-ray observation. The lack of star formation in this galaxy has led to the conclusion that this diffuse X-ray gas is externally accreted gas now cooling in an extended hot halo [112].

Table 5.33: Fit parameters: NGC 5746

model parameter	unit	value
powerlaw Index		1.93± 1.28
powerlaw normalisation		$1.35 \times 10^{-5} \pm 1.7 \times 10^{-5}$
mekal kT	keV	1.01 ± 0.76
mekal nH	cm^{-3}	6.1×10^{-6} (frozen)
mekal Abundance		1.0 (frozen)
mekal redshift		5.7×10^{-3} (frozen)
mekal normalisation		$7.8 \times 10^{-6} \pm 2.4 \times 10^{-6}$

NGC 5775

NGC 5775 is a barred spiral interacting with NGC 5774. Observations suggest that the galaxies are in early stages of merger [70].

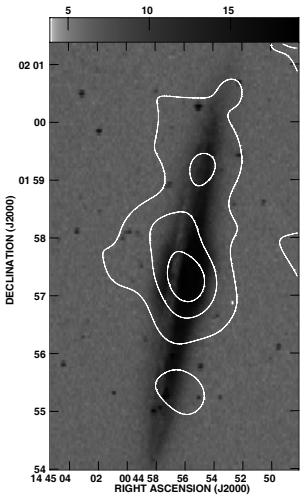

Figure 5.75: NGC 5746

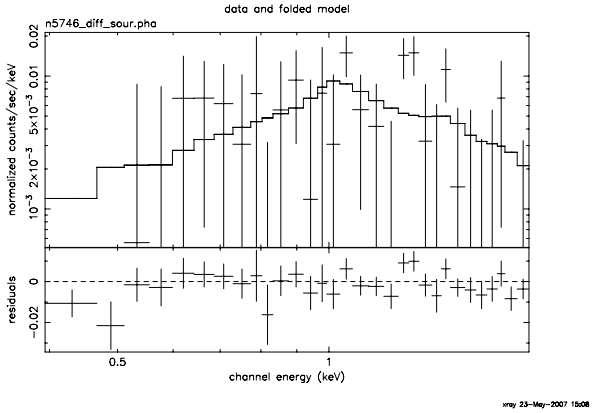

Figure 5.76: X-ray spectra (0.3 - 2.0 keV) of NGC 5746

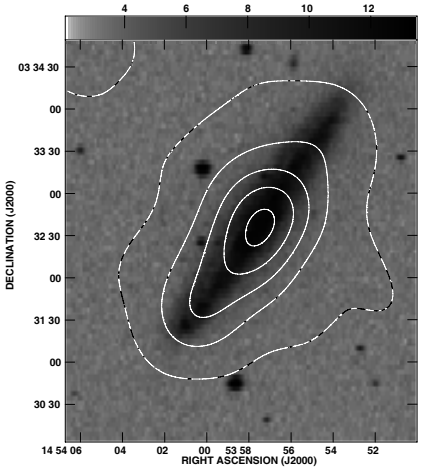

Figure 5.77: NGC 5775

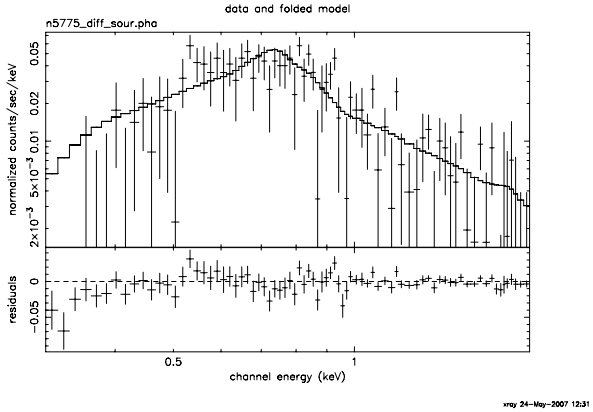

Figure 5.78: X-ray spectra (0.3 - 2.0 keV) of NGC 5775

Table 5.34: Fit parameters: NGC 5775

model parameter	unit	value
powerlaw Index		2.05 ± 0.31
powerlaw normalisation		$1.96\times10^{-5} \pm 0.50\times10^{-5}$
mekal kT	keV	0.26 ± 0.03
mekal nH	cm^{-3}	6.4×10^{-6} (frozen)
mekal Abundance		1.0 (frozen)
mekal redshift		5.6×10^{-3} (frozen)
mekal normalisation		$1.22\times10^{-5} \pm 0.51\times10^{-5}$

NGC 5879

NGC 5879 is a nearby spiral hosting a low luminosity AGN.

Table 5.35: Fit parameters: NGC 5879

model parameter	unit	value
powerlaw Index		3.42±0.66
powerlaw normalisation		$1.83\times10^{-6} \pm 2.00\times10^{-6}$
mekal kT	keV	0.42±0.09
mekal nH	cm^{-3}	3.71×10^{-6} (frozen)
mekal Abundance		1.0 (frozen)
mekal redshift		2.57×10^{-3} (frozen)
mekal normalisation		$1.92\times10^{-6} \pm 1.03\times10^{-6}$

NGC 6503

NGC 6503 is a late type, nearly spiral. This is a low mass object for its type. H I in it is centrally concentrated and large scale H I distribution is asymmetric. Though the projected distance between NGC 6503 and a nearly quasar is very small, studies indicate that this galaxy is not physically associated to the quasar [128].

NGC 7331

NGC 7331 is a nearby spiral of the NGC 7320 group. It is referred to as a post-starburst galaxy in literature. The galaxy has a central hole in the molecular gas distribution which

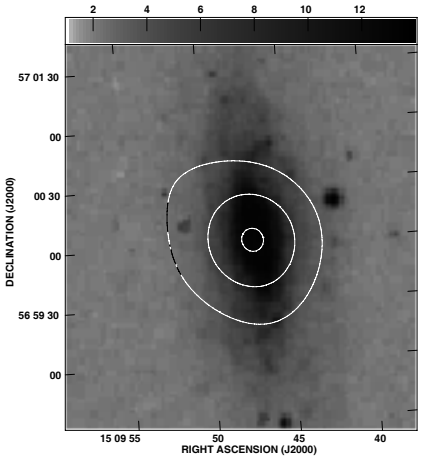

Figure 5.79: NGC 5879

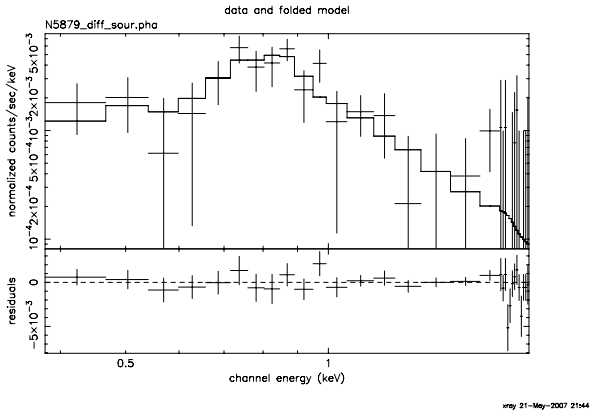

Figure 5.80: X-ray spectra (0.3 - 2.0 keV) of NGC 5879

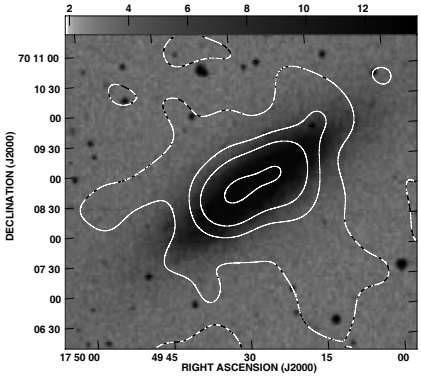

Figure 5.81: NGC 6503

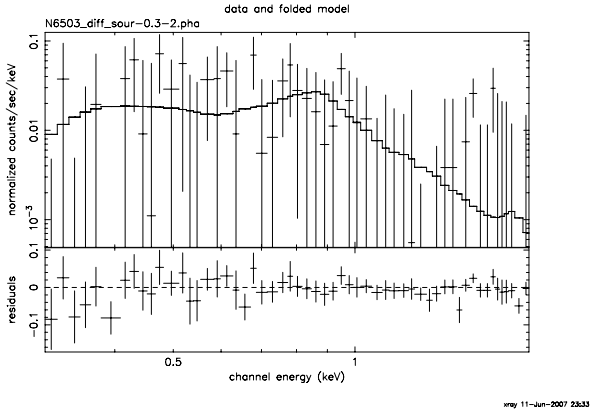

Figure 5.82: X-ray spectra (0.3 - 2.0 keV) of NGC 6503

Table 5.36: Fit parameters: NGC 6503

model parameter	unit	value
powerlaw Index		3.01±2.61
powerlaw normalisation		$5.54 \times 10^{-5} \pm 0.267 \times 10^{-4}$
mekal kT	keV	0.577 ± 0.26
mekal nH	cm^{-3}	2.100×10^{-5} (frozen)
mekal Abundance		1.0 (frozen)
mekal redshift		2.000×10^{-4} (frozen)
mekal normalisation		$8.27 \times 10^{-6} \pm 0.21 \times 10^{-4}$

could have occurred due to the gas consumption over the long evolution after the past starburst event [145].

Table 5.37: Fit parameters: NGC 7331

model parameter	unit	value
powerlaw Index		1.81 ±0.23
powerlaw normalisation		$5.84 \times 10^{-5} \pm 0.12 \times 10^{-4}$
mekal kT	keV	0.412 ± 0.058
mekal nH	cm^{-3}	2.150×10^{-5} (frozen)
mekal Abundance		1.0 (frozen)
mekal redshift		2.722×10^{-3} (frozen)
mekal normalisation		$1.55 \times 10^{-5} \pm \times 10^{-5}$

NGC 7714

NGC 7714 is a spiral galaxy interacting with another spiral NGC 7715. H I observations show massive bridge connecting the two galaxies. Redshifted H I absorption toward the NGC 7714 nucleus, suggest infall onto the starburst nucleus [130].

NGC 7727

NGC 7727 is a post-merger galaxy. The morphology of NGC 7727 (Arp 222) in the optical and near infrared suggests that it is the product of a merger of two disk galaxies after approximately 1 Gyr that will become an elliptical galaxy [35].

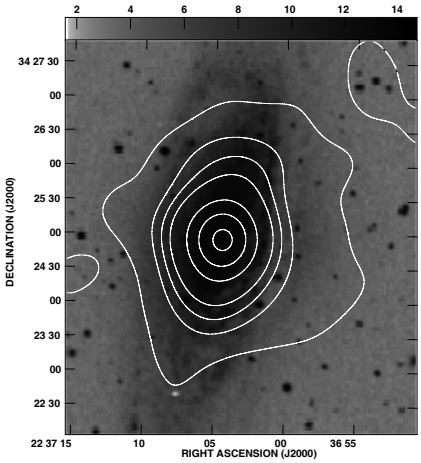

Figure 5.83: NGC 7331

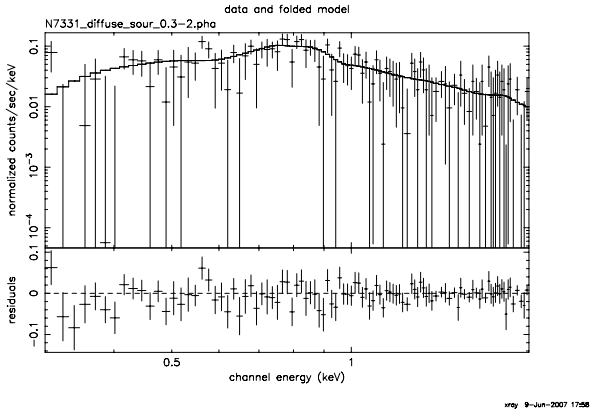

Figure 5.84: X-ray spectra (0.3 - 2.0 keV) of NGC 7331

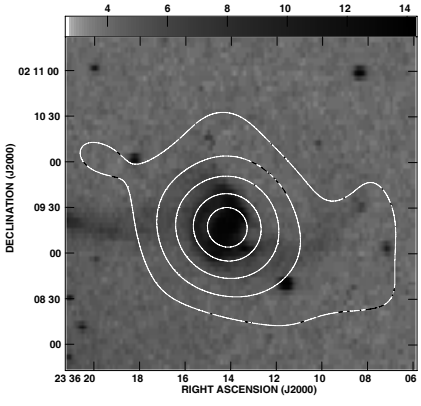

Figure 5.85: NGC 7714

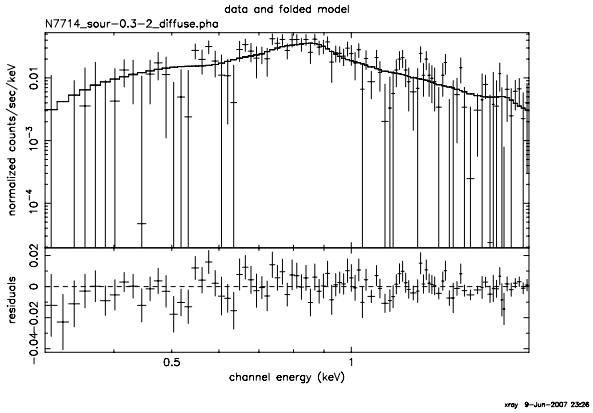

Figure 5.86: X-ray spectra (0.3 - 2.0 keV) of NGC 7714

Table 5.38: Fit parameters: NGC 7714

model parameter	unit	value
powerlaw Index		1.94± 0.230
powerlaw normalisation		$1.92\times10^{-5} \pm 0.47\times10^{-5}$
mekal kT	keV	0.536± 0.037
mekal nH	cm^{-3}	5.3×10^{-6} (frozen)
mekal Abundance		1.0 (frozen)
mekal redshift		9.33×10^{-3} (frozen)
mekal normalisation		$9.79 \times10^{-6} \pm 0.45\times10^{-5}$

Table 5.39: Fit parameters: NGC 7727

model parameter	unit	value
powerlaw Index		2.32 ± 0.45
powerlaw normalisation		$8.70 \times10^{-6} \pm 0.67 \times10^{-5}$
mekal kT	keV	0.655± 0.0641
mekal nH	cm^{-3}	4.600×10^{-6} (frozen)
mekal Abundance		1.0 (frozen)
mekal redshift		6.23×10^{-3} (frozen)
mekal normalisation		$9.09 \times10^{-6} \pm 0.69\times10^{-5}$

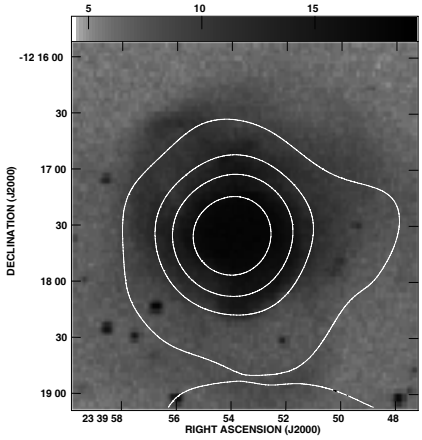

Figure 5.87: NGC 7727

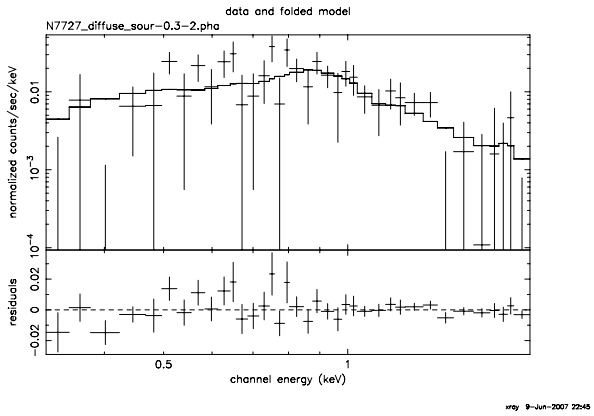

Figure 5.88: X-ray spectra (0.3 - 2.0 keV) of NGC 7727